A novel POD-based ROM strategy for the prediction in time of advection-dominated problems

P. Solán-Fustero[*,‡], J.L. Gracia[†], A. Navas-Montilla[*], P. García-Navarro[*]

Abstract

The use of reduced-order models (ROMs) for the numerical approximation of the solution of partial differential equations is a topic of current interest, being motivated by the high computational efficiency of ROMs when compared to full-order models (FOMs). To construct a ROM to approximate the solution of transport equations, the use of the proper orthogonal decomposition (POD) method is a common choice. POD-based ROMs rely on the snapshot method, which consists in the off-line computation of a set of values corresponding to the solution up to the training time by means of the FOM. Then, the ROM is constructed and solved, up to the training time. When considering parabolic equations, the method is able to compute the solution beyond the training time. However, when considering hyperbolic problems, POD-based ROMs fail when computing the solution beyond the training time, this being one of the strongest limitations of POD-based ROMs. In this work, a novel strategy in the framework of POD-based ROMs to extrapolate solutions in time is introduced. This method, called CT-ROM, is based on a coordinate transformation and allows to compute the solution of advection-dominated problems beyond the training time. The performance of this novel strategy is assessed using a variety of test cases, showing promising results in all of them. The extension of the CT-ROM to higher spatial dimensions by means of the Radon transform is also presented. The results obtained are encouraging and motivate the application of this idea to more complex problems.

Keywords: Reduced-order modelling; POD methods; snapshots method; computational resources; time extrapolation

Contents

[*]I3A and Fluid Mechanics Department, University of Zaragoza, Spain.
[†]IUMA and Department of Applied Mathematics, University of Zaragoza, Spain.
[‡]Corresponding author (psolfus@unizar.es)

1. Introduction

Many of the problems considered in Fluid Mechanics are modelled by systems of partial differential equations that stand for the conservation of some fundamental magnitudes (e.g. mass, momentum, energy, etc.), often including source terms that increase their complexity. The solutions of such equations cannot be obtained analytically and are generally approached by means of numerical methods, such as the finite volume method, the finite difference method or finite element method (such as the discontinuous Galerkin method) among others, which allow to compute the evolution in time of the flow variables inside the computational domain.

The transient nature of real flows and the increasing need for higher fidelity solutions entail a high cost of computational resources, including computing power, storage capacity and interconnection. When computing realistic events of long duration, i.e., the length of the event is much longer than the time scales of the relevant features of the flow, the need to speed up computational time is essential to preserve the predictive nature of the tool. The large number and diversity of problems requiring computational cost improvement has led in recent years to the development of a wide range of mathematical strategys and tools, including the (discrete) empirical interpolation method [6, 9], the dynamic mode decomposition [2, 43], the Krylov subspaces method [13] and artificial neural networks [2], among many others.

In addition to the above methods, the reduced-order model (ROM) strategy is one of the most popular in the field. It was originally developed as the Reduced basis strategy for predicting the nonlinear static response of structures [5, 29, 32]. The ROM strategy states that the variable of interest resides on a low-dimensional manifold within the infinite-dimensional solution space associated with the partial differential equation [35].

Proper orthogonal decomposition (POD), which is one of the most significant methodologies related to ROM in Fluid Mechanics [3], was introduced originally by Lumley in 1967 [27] to approach the turbulence problem by random field of velocities of turbulent flows into a set of deterministic functions [47]. The POD method is also known as Karhunen-Loève expansions [24, 26], principal component analysis [34, 23]. There are different modified POD methods proposed in the literature, such as the weighted POD [10], proper interval decomposition [1, 7, 22, 48], spectral POD [46] and manifold approximations via transported subspaces [40].

The procedure of solving a problem with the POD-based ROM strategy starts with the snapshot method [44], which consists of the off-line computation of a set of values corresponding to the solution up to the training time by means a numerical scheme that is called the full-order model (FOM). These snapshots are used to train the ROM in the so-called on-line part. Then, the ROM can be solved up to the training time, thus setting up an interpolation problem or beyond that time horizon, if possible. In this case, one of the advantages of the ROM is that a speed-up of several orders of magnitude is possible [1].

The computation of the solution beyond the training time is not always possible and represents one of the major limitations of the POD method when dealing with advection-dominated equations [1], this being a challenging problem of recent interest. Computing extrapolated solutions with a ROM for times longer than the training time would suppose a major step in the field of computational hydraulics. For this reason, a new ROM strategy based on a coordinate transformation [19], which is called CT-ROM, is proposed in this work with the aim of predicting solutions beyond the training time.

ROMs have been developed in the literature for elliptic [35], parabolic [20, 21, 41] and hyperbolic equations including the linear scalar equation [37], as well as for the Burgers equation [1, 31, 40, 42], the Navier-Stokes equations [7, 21], the shallow water equations (SWE) [2, 48] and other nonlinear problems involving discontinuous solutions [45]. There are different formulations of POD-based ROMs according to their relation with the FOM, as they can be intrusive [5, 31, 48] and non-intrusive [1]. In this work, the CT-ROM is applied intrusively to the 1D linear advection-diffusion-reaction equation and to 1D linear hyperbolic systems of partial differential equations, namely the linearized SWE and a solute transport coupled model. The application of the CT-ROM to nonlinear problems such as the Burgers equation is also explored. The FOMs of these equations are constructed by means of the standard Godunov first-order upwind method [4, 16, 17].

The CT-ROM herein introduced is a genuinely 1D method. An extension of this strategy to 2D problems by means of the Radon transform is also presented [38]. This extension is based on the intertwining property of the Radon transform, which allows to express the 2D problem as a collection of 1D problems, all of them written in terms of a univariate derivative [12, 39, 40]. Then, the CT-ROM strategy can be applied to each of those 1D problems, and the solution in the 2D physical domain is computed by means of a back-projection, i.e., the inverse Radon transform. This approach proves useful for the application of the CT-ROM method to hyperbolic partial differential equations in 2D. Results for the computation of a 2D advection problem are presented.

The remainder of the paper is organized as follows. Section 2 describes the standard POD-based ROM strategy, showing with an example the flaw of this method when predicting beyond the training time. Section 3 introduces the novel CT-ROM strategy and presents some examples of application to linear and non-linear problems. The extension to 2D problems is also included in this section. Finally, concluding remarks are drawn in Section 4.

2. ROM strategy

Consider the following partial differential equation

$$\frac{\partial u(x,t)}{\partial t}+\frac{\partial f(u(x,t))}{\partial x}=\nu\frac{\partial^2 u(x,t)}{\partial x^2}-cu(x,t),\;\;(x,t)\in(0,L)\times(0,T]\,, \qquad (1)$$

where $f(u(x,t))$ is the physical flux; $\nu \geq 0$ is the diffusion coefficient; and c is the reaction coefficient. The initial (IC) and boundary (BC) conditions considered will be indicated for each specific problem.

In the present work, the FOM to approximate the solution of problem (1) is based on the Finite volume (FV) method. The computational domain is discretized by means of volume cells of uniform length Δx and the positions of the center and left and right interfaces of j-th cell are x_j, $x_{j-1/2}$ and $x_{j+1/2}$, respectively, with $j=1,...,N_x$. Regarding the time discretization, the time step $\Delta t = t^{n+1}-t^n$ with $n=0,...,N_{train}$, is selected dynamically using the Courant-Friedrichs-Lewy (CFL) condition [11] as follows

$$\Delta t = CFL\frac{\Delta x^2}{\Delta x \max\left(\lambda\right)+2\nu},$$

where $\lambda = \dfrac{\partial f}{\partial u}$ and $CFL < 1$. The FOM is formulated by means of the FV method [25, 33]

$$\frac{u_j^{n+1} - u_j^n}{\Delta t} + \frac{\delta f_{j+1/2}^{n,-,*} + \delta f_{j-1/2}^{n,+,*}}{\Delta x} = \nu \frac{u_{j+1}^n - 2u_j^n + u_{j-1}^n}{\Delta x^2} - c u_j^n, \tag{2}$$

where $u_j^n \approx u(x_j, t^n)$ is the cell average value over the cell $(x_{j-1/2}, x_{j+1/2})$ and $\delta f_{j\pm 1/2}^{n,\mp,*}$ are the numerical flux differences, defined as

$$\delta f_{j\pm 1/2}^{n,\mp,*} = \left(\bar{\lambda}^{\mp} \delta u\right)_{j\pm 1/2}^n, \tag{3}$$

with $\delta u_{j+1/2}^n = u_{j+1}^n - u_j^n$ and

$$\left(\bar{\lambda}^{\pm}\right)_{j+1/2}^n = \frac{1}{2}\left(\bar{\lambda} \pm |\bar{\lambda}|\right)_{j+1/2}^n, \tag{4}$$

where $\bar{\lambda}_{j+1/2}^n$ is the approximate wave celerity at time t^n and cell interface $x_{j+1/2}$.

Numerical approximations to the solution $u(x,t)$ are computed with (2) up to a training time $t_{train} = t^{N_{train}}$ with $t_{train} \leq T$. It is considered a prediction or extrapolation in time when the ROM computes the approximate solution of $u(x,t)$ at $t > t_{train}$, being particularly interesting the case when $t_{train} \ll T$.

A set of N_{train} time numerical solutions, also called snapshots u_j^n, is used to construct the snapshot matrix $\mathbf{U} \in \mathbb{R}^{N_x \times N_{train}}$

$$\mathbf{U} = \begin{pmatrix} u_1^1 & u_1^2 & \cdots & u_1^{N_{train}} \\ u_2^1 & u_2^2 & \cdots & u_2^{N_{train}} \\ \vdots & \vdots & \ddots & \vdots \\ u_{N_x}^1 & u_{N_x}^2 & \cdots & u_{N_x}^{N_{train}} \end{pmatrix}.$$

A basis of functions is calculated by applying the singular value decomposition (SVD, [18]) to the snapshot matrix

$$\mathbf{U} = \mathbf{\Phi}\mathbf{\Sigma}\mathbf{\Psi}^T,$$

where $\mathbf{\Sigma} \in \mathbb{R}^{N_x \times N_{train}}$ is a diagonal matrix whose entries of the main diagonal are the singular values of $\mathbf{U}$ and $\mathbf{\Phi} \in \mathbb{R}^{N_x \times N_x}$ and $\mathbf{\Psi} \in \mathbb{R}^{N_{train} \times N_{train}}$ are orthogonal matrices. The matrix $\mathbf{\Phi} = (\phi_1, \ldots, \phi_{N_x})$ with $\phi_k = (\phi_{1,k}, \ldots, \phi_{N_x,k})^T$ consists of the orthogonal eigenvectors of $\mathbf{U}\mathbf{U}^T$.

Let N_{POD} be a positive integer such that $N_{\text{POD}} \leq N_{train}$ and it will be chosen as small as possible without significantly affecting the accuracy of the computed solution with our reduced order method. The POD basis $\{\phi_1, ..., \phi_{N_{\text{POD}}}\}$ of dimension N_{POD} is used to construct, in the offline stage, a set of matrices that are fed into the ROM. In the online stage, the reduce-order approximations $\hat{\mathbf{v}}^n = (\hat{v}_1^n, \ldots, \hat{v}_{N_{\text{POD}}}^n)^T$ for $t^n > t_{train}$ are computed with the POD-based reduced-order finite volume method. Then, the numerical solution $v(x_j, t^n)$ is reconstructed using the Galerkin projection [14]

$$v_j^n = \sum_{p=1}^{N_{\text{POD}}} \hat{v}_p^n \phi_{j,p}, \ j = 1, ..., N_x. \tag{5}$$

Bounds on the difference between $\mathbf{u}^n$ and its orthogonal projection onto span$\{\phi_1, ..., \phi_{N_{\mathrm{POD}}}\}$ when $t^n \leq t_{train}$ are available in the literature (see, for example, [36, Theorem 6.1]), but not when $t^n > t_{train}$. In the following section a simple 1D linear problem is considered and it is shown that a standard POD-based ROM does not provide accurate approximations to the solution when $t > t_{train}$.

Performance of standard POD-based ROM: 1D linear advection-diffusion problem

Consider the 1D linear equation (1) where the physical flux is $f(u(x,t)) = au(x,t)$ and the approximate wave celerity in (2) is $\bar{\lambda}^n_{j+1/2} = a$, $\forall j, n$.

The intrusive ROM of (2) is obtained by: i) introducing the Galerkin method (5) into the FOM; ii) multiplying it by $\phi_{j,p}$ (the p-th component of the vector ϕ_j of the POD basis); and iii) summing up over the cells (i.e., from $j = 1$ to N_x). For a full development of the procedure to obtain the ROM, see [48].

The vector formulation of the ROM of the 1D linear advection-diffusion problem is

$$\hat{\mathbf{v}}^{n+1} = \hat{\mathbf{v}}^n - \frac{a}{2}\frac{\Delta t}{\Delta x}A\hat{\mathbf{v}}^n + \frac{|a|}{2}\frac{\Delta t}{\Delta x}B\hat{\mathbf{v}}^n + \nu\frac{\Delta t}{\Delta x^2}B\hat{\mathbf{v}}^n - c\Delta t C\hat{\mathbf{v}}^n, \tag{6}$$

where the elements of matrices $A = (A_{kp})$, $B = (B_{kp})$ and $C = (C_{kp}) \in \mathbb{R}^{N_{POD}\times N_{POD}}$ are

$$\begin{aligned}
A_{kp} &= \Lambda^1_{kp} + \sum_{j=2}^{N_x-1}\left[\phi_{j+1,k} - \phi_{j-1,k}\right]\phi_{j,p} + \Lambda^{N_x}_{kp},\\
B_{kp} &= \beta^1_{kp} + \sum_{j=2}^{N_x-1}\left[\phi_{j+1,k} - 2\phi_{j,k} + \phi_{j-1,k}\right]\phi_{j,p} + \beta^{N_x}_{kp},\\
C_{kp} &= \zeta^1_{kp} + \sum_{j=2}^{N_x-1}\phi_{j,k}\phi_{j,p} + \zeta^{N_x}_{kp},
\end{aligned}$$

and the terms Λ^1_{kp}, $\Lambda^{N_x}_{kp}$, β^1_{kp}, $\beta^{N_x}_{kp}$, ζ^1_{kp} and $\zeta^{N_x}_{kp}$ depend on the type of the boundary conditions. For example, in the case of Dirichlet boundary conditions, they are given by

$$\begin{aligned}
&\Lambda^1_{kp} = \left(\phi_{2,k} - \phi_{1,k}\right)\phi_{1,p}, \quad && \Lambda^{N_x}_{kp} = \left(\phi_{N_x,k} - \phi_{N_x-1,k}\right)\phi_{N_x,p},\\
&\beta^1_{kp} = \left(\phi_{2,k} - \phi_{1,k}\right)\phi_{1,p}, \quad && \beta^{N_x}_{kp} = \left(\phi_{N_x,k} - \phi_{N_x-1,k}\right)\phi_{N_x,p},\\
&\zeta^1_{kp} = 0, && \zeta^{N_x}_{kp} = 0,
\end{aligned} \tag{7}$$

and, if periodic boundary conditions are considered, then

$$\begin{aligned}
&\Lambda^1_{kp} = \left(\phi_{2,k} - \phi_{N_x,k}\right)\phi_{1,p}, && \Lambda^{N_x}_{kp} = \left(\phi_{1,k} - \phi_{N_x-1,k}\right)\phi_{N_x,p},\\
&\beta^1_{kp} = \left(\phi_{2,k} - 2\phi_{1,k} + \phi_{N_x,k}\right)\phi_{1,p}, \quad && \beta^{N_x}_{kp} = \left(\phi_{1,k} - 2\phi_{N_x,k} + \phi_{N_x-1,k}\right)\phi_{N_x,p},\\
&\zeta^1_{kp} = 0, && \zeta^{N_x}_{kp} = 0.
\end{aligned} \tag{8}$$

The ROM (6) is used to approximate the advection-diffusion problem (1) with $\nu = 0.001$, $a = 0.5$ and $c = 0$. In the domain $[0, 2] \times [0, 0.5]$, with IC

$$u(x, 0) = 1 + e^{-200(x-1)^2}, \quad 0 < x < 2, \tag{9}$$

and BC

$$u(0,t) = u(2,t) = 1, \quad 0 \leq t \leq 0.5. \tag{10}$$

The spatial domain is divided into $N_x = 200$ volume cells of cell size $\Delta x = 0.01$. The time step, with $CFL = 0.9$, is

$$\Delta t = CFL \frac{\Delta x^2}{a\Delta x + 2\nu} = 0.0129,$$

Numerical approximations to $u(x,t)$ have been computed with the FOM (2) up to $t_{train} = 0.1$ which corresponds with $N_{train} = 9$. From these data, new numerical approximations are computed using the ROM (6) up to the final time $T = 0.5$. Figure 1 plots numerical results for this example with $N_{\text{POD}} = 14$: Figures 1a and 1b show the time evolution of the Gaussian IC computed by the FOM and the ROM, respectively; Figure 1c shows the same ROM results superimposed on top of each other. It can be seen in Figures 1b and 1c that the ROM, for times greater than the training time, generates fluctuations in the solution that blur the Gaussian profile, so it ends up not resembling the reference solution at the final time $T = 0.5$ (red line). This can be seen in Figure 1d, where the ROM solution is compared with the FOM solution at $T = 0.5$. It also includes the IC and the FOM solution at the training time ($t_{train} = 0.1$).

It should be noted that for diffusion-dominated problems, extrapolation in time can be done with the standard ROM. However, this example justifies the development of a new ROM strategy to predict solutions beyond the training time for advection-dominated problems.

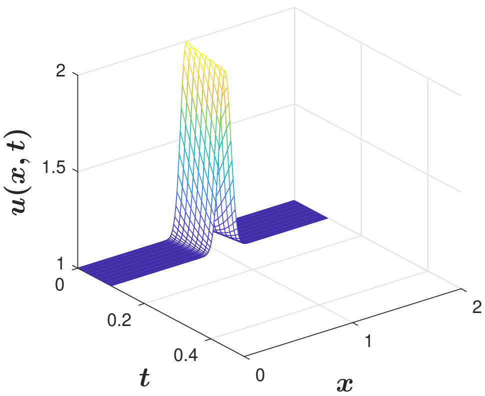

(a) Solution computed with the FOM.

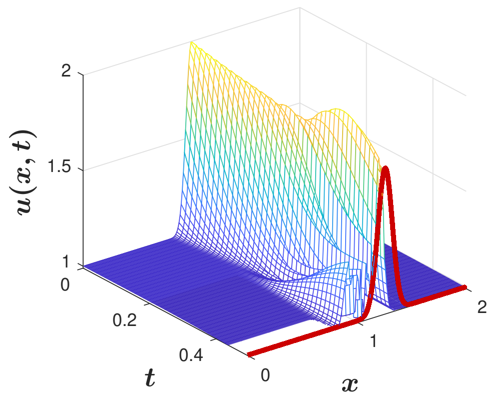

(b) Solution computed with the ROM.

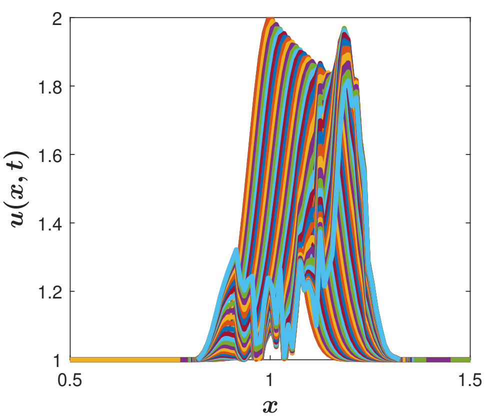

(c) Solution computed with the ROM.

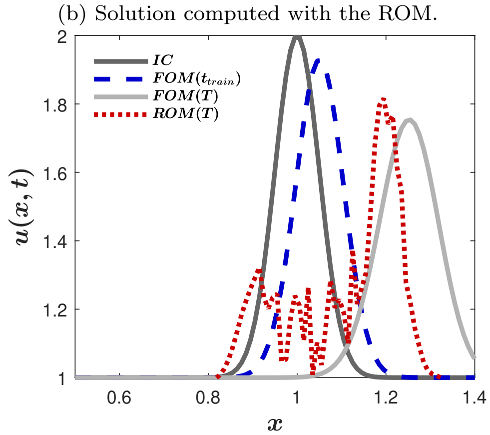

(d) Comparison between the FOM and the ROM results.

Figure 1: Solutions computed with the FOM/ROM.

3. CT-ROM strategy

In this section, a new ROM (which is called in this paper CT-ROM) is presented based on an appropriate coordinate transformation and the POD to generate accurate approximations to (1) beyond the training time. For that purpose, an interior point $d^0 \in (0, L)$ must be identified in the initial condition, such as, for example, the peak of a Gaussian function or a discontinuity. Our CT-ROM approximates the solution in a new coordinate system which is aligned with the characteristic curve emanating from point d^0. This strategy is applied to some cases. First, the case of a linear problem with $f(u(x,t)) = a(t)u(x,t)$ is considered and later the extension to the Burgers' equation is outlined.

3.1. CT-ROM applied to 1D linear problems

Consider the characteristic curve $d(t)$ defined by

$$d'(t) = a(t), \; 0 < t \leq T, \quad d(0) = d^0. \tag{11}$$

It is given by

$$d(t) = \int_{s=0}^{t} a(s)\, ds + d(0),$$

and it is assumed that $d(T) < L$. This characteristic curve is used to define the following mapping [19]:

$$\tilde{x}(t) = \begin{cases} \dfrac{d(0)}{d(t)} x, & \text{if } 0 \leq x \leq d(t), \\ L - \dfrac{L - d(0)}{L - d(t)}(L - x), & \text{if } d(t) < x \leq L. \end{cases} \tag{12}$$

Note that the sub-domains $\{(x,t),\, 0 \leq x \leq d(t),\, 0 \leq t \leq T\}$ and $\{(x,t),\, d(t) \leq x \leq L,\, 0 \leq t \leq T\}$ are transformed into the rectangular sub-domains $[0, d(0)] \times [0, T]$ and $[d(0), L] \times [0, T]$, respectively. In addition, note that $\tilde{x} = x$ at $t = 0$. Using the chain rule

$$\frac{\partial u}{\partial x} = \begin{cases} \dfrac{d(0)}{d(t)} \dfrac{\partial \tilde{u}}{\partial \tilde{x}}, & \text{if } 0 < x < d(t), \\ \dfrac{L - d(0)}{L - d(t)} \dfrac{\partial \tilde{u}}{\partial \tilde{x}}, & \text{if } d(t) < x < L, \end{cases}$$

and

$$\frac{\partial u}{\partial t} = \begin{cases} \dfrac{\partial \tilde{u}}{\partial t} - a(t) \dfrac{\tilde{x}}{d(t)} \dfrac{\partial \tilde{u}}{\partial \tilde{x}}, & \text{if } 0 < x < d(t), \\ \dfrac{\partial \tilde{u}}{\partial t} - a(t) \dfrac{L - \tilde{x}}{L - d(t)} \dfrac{\partial \tilde{u}}{\partial \tilde{x}}, & \text{if } d(t) < x < L. \end{cases}$$

Thus, the following problem is obtained when the mapping (12) is applied to (1) with $f(u(x,t)) = a(t)u(x,t)$

$$\begin{cases} \dfrac{\partial \tilde{u}}{\partial t} + \left[a(t) \dfrac{d(0)}{d(t)} - a(t) \dfrac{\tilde{x}}{d(t)} \right] \dfrac{\partial \tilde{u}}{\partial \tilde{x}} = \nu \left(\dfrac{d(0)}{d(t)} \right)^2 \dfrac{\partial^2 \tilde{u}}{\partial \tilde{x}^2} - c\tilde{u}, & \text{if } 0 < \tilde{x} < d(0), \\ \dfrac{\partial \tilde{u}}{\partial t} + \left[a(t) \dfrac{L - d(0)}{L - d(t)} - a(t) \dfrac{L - \tilde{x}}{L - d(t)} \right] \dfrac{\partial \tilde{u}}{\partial \tilde{x}} = \nu \left(\dfrac{L - d(0)}{L - d(t)} \right)^2 \dfrac{\partial^2 \tilde{u}}{\partial \tilde{x}^2} - c\tilde{u}, & \text{if } d(0) < \tilde{x} < L, \end{cases} \tag{13}$$

where $\tilde{u}(\tilde{x}, t) = u(x, t)$. In the following it is assumed that the solution $\tilde{u}$ of (13) is a smooth function in $[0, L] \times [0, T]$.

In the transformed variables $(\tilde{x}, t)$, the computational mesh is rectangular, but in the physical variables (x, t), it is a time dependent mesh which is aligned with the characteristic curve $d(t)$. The spatial mesh in the transformed domain is uniform in the subintervals $[0, d(0)]$ and $[d(0), L]$ with $\tilde{x}_{J+1/2} = d(0)$. The coordinate transformed FOM (CT-FOM) is defined on this mesh and it is given by

$$\begin{cases} \tilde{u}_j^{n+1} & = \tilde{u}_j^n - \dfrac{\Delta t}{\Delta x} \left[\dfrac{d^0}{d^n} \left(\delta \tilde{f}_{j+1/2}^{n,-,*} + \delta \tilde{f}_{j-1/2}^{n,+,*} \right) - \dfrac{a^n}{d^n} \left(\delta \tilde{f}_{j+1/2}^{n,-,**} + \delta \tilde{f}_{j-1/2}^{n,+,**} \right) \right] \\ & \quad + \nu \dfrac{\Delta t}{\Delta \tilde{x}^2} \left(\dfrac{d^0}{d^n} \right)^2 \left(\tilde{u}_{j+1}^n - 2\tilde{u}_j^n + \tilde{u}_{j-1}^n \right) - \Delta t c \tilde{u}_j^n, \quad \text{if } \tilde{x}_j \leq d^0, \\ \\ \tilde{u}_j^{n+1} & = \tilde{u}_j^n - \dfrac{\Delta t}{\Delta x} \left[\dfrac{L - d^0}{L - d^n} \left(\delta \tilde{f}_{j+1/2}^{n,-,*} + \delta \tilde{f}_{j-1/2}^{n,+,*} \right) - \dfrac{a^n}{L - d^n} \left(\delta \tilde{f}_{j+1/2}^{n,-,**} + \delta \tilde{f}_{j-1/2}^{n,+,**} \right) \right] \\ & \quad + \nu \dfrac{\Delta t}{\Delta \tilde{x}^2} \left(\dfrac{L - d^0}{L - d^n} \right)^2 \left(\tilde{u}_{j+1}^n - 2\tilde{u}_j^n + \tilde{u}_{j-1}^n \right) - \Delta t c \tilde{u}_j^n, \quad \text{if } \tilde{x}_j > d^0, \end{cases} \tag{14}$$

where $a^n = a(t^n)$, $d^n = d(t^n)$ and the numerical fluxes are

$$\delta \tilde{f}_{j+1/2}^{n,\pm,*} = \left(\bar{\lambda}_{j+1/2}^{\pm,*} \delta \tilde{u}_{j+1/2} \right)^n, \quad \delta \tilde{f}_{j+1/2}^{n,\pm,**} = \left(\bar{\lambda}_{j+1/2}^{\pm,**} \delta \tilde{u}_{j+1/2} \right)^n,$$

with $\delta\tilde{u}^n_{j+1/2} = \tilde{u}^n_{j+1} - \tilde{u}^n_j$, and

$$\begin{aligned}
\bar{\lambda}^{n,\pm,*}_{j+1/2} &= \frac{1}{2}\left(\bar{\lambda}^{n,*}_{j+1/2} \pm \left|\bar{\lambda}^{n,*}_{j+1/2}\right|\right) = \frac{1}{2}\left(a^n \pm |a^n|\right),\\
\bar{\lambda}^{n,+,**}_{j+1/2} &= \frac{1}{2}\left(\bar{\lambda}^{n,**}_{j+1/2} + \left|\bar{\lambda}^{n,**}_{j+1/2}\right|\right) = \begin{cases}\tilde{x}_{j+1/2}\,, & \text{if } \tilde{x}_j \le d^0,\\ L - \tilde{x}_{j+1/2}, & \text{if } \tilde{x}_j > d^0,\end{cases}\\
\bar{\lambda}^{n,-,**}_{j+1/2} &= \frac{1}{2}\left(\bar{\lambda}^{n,**}_{j+1/2} - \left|\bar{\lambda}^{n,**}_{j+1/2}\right|\right) = 0.
\end{aligned}$$

The explicit updating equation of the reduced order model with the coordinate transformation (CT-ROM) is obtained following the same three steps indicated in the previous section for the POD method. The reduced-order solution approximations of the CT-ROM are $\hat{\mathbf{w}}^n = (\hat{w}^n_1, \ldots, \hat{w}^n_{N_{\mathrm{POD}}})^T$ and the CT-ROM itself

$$\begin{aligned}
\hat{\mathbf{w}}^{n+1} = {}& \hat{\mathbf{w}}^n - \frac{1}{2}a^n\frac{\Delta t}{\Delta\tilde{x}}\left[\frac{d^0}{d^n}A^L + \frac{L-d^0}{L-d^n}A^R\right]\hat{\mathbf{w}}^n + \frac{1}{2}|a^n|\frac{\Delta t}{\Delta\tilde{x}}\left[\frac{d^0}{d^n}B^L + \frac{L-d^0}{L-d^n}B^R\right]\hat{\mathbf{w}}^n\\
& + \frac{1}{4}a^n\frac{\Delta t}{\Delta\tilde{x}}\left[\frac{1}{d^n}D^L + \frac{1}{L-d^n}D^R\right]\hat{\mathbf{w}}^n + \nu\frac{\Delta t}{\Delta\tilde{x}^2}\left[\left(\frac{d^0}{d^n}\right)^2 B^L + \left(\frac{L-d^0}{L-d^n}\right)^2 B^R\right]\hat{\mathbf{w}}^n\\
& - c\Delta t C\hat{\mathbf{w}}^n,
\end{aligned} \tag{15}$$

where the elements of these matrices are

$$\begin{aligned}
&A^L_{kp} = \Lambda^1_{kp} + \sum_{j=2}^{J}\left(\phi_{j+1,k} - \phi_{j-1,k}\right)\phi_{j,p},\ B^L_{kp} = \beta^1_{kp} + \sum_{j=1}^{J}\left(\phi_{j+1,k} - 2\phi_{j,k} + \phi_{j-1,k}\right)\phi_{j,p},\\
&C_{kp} = \zeta^1_{kp} + \sum_{j=2}^{N_x-1}\phi_{j,k}\phi_{j,p} + \zeta^{N_x}_{kp},\ D^L_{kp} = \delta^1_{kp} + 4\sum_{j=2}^{J}\tilde{x}_{j-1/2}\left(\phi_{j,k} - \phi_{j-1,k}\right)\phi_{j,p},\ D^R_{kp} = \delta^{N_x}_{kp},
\end{aligned}$$

where J is the position of the adjacent cell to $\tilde{x}_{J+1/2} = d(0)$, and the terms Λ^1_{kp}, β^1_{kp}, ζ^1_{kp} and $\zeta^{N_x}_{kp}$ are given in (7) and (8) for Dirichlet and periodic BC, respectively. The matrices A^R and B^R are defined similarly to A^L and B^L and the limits of the summations are from $j = J+1$ to $N_x - 1$. The terms δ^1_{kp} and $\delta^{N_x}_{kp}$ in the matrices D^L and D^R are obtained following the same procedure. Once $\hat{\mathbf{w}}^n$ is computed with (15) at all the times levels t^n, $n = 0, 1, \ldots, N_T$, the numerical approximation w^n_j at the mesh points $\{(x_j, t_n),\ j = 1, 2, \ldots, N_x,\ n = 0, 1, \ldots, N_T\}$ of the physical domain is generated

$$w^n_j = \sum_{p=1}^{N_{\mathrm{POD}}}\hat{w}^n_p\phi_{j,p},\ j = 1, ..., N_x.$$

The CT-ROM outlined above is applied to four numerical cases.

Case 1. 1D transport of Gaussian IC

The example described in Section 2 is revisited and the ability of the ROM and the CT-ROM to predict solutions beyond the training time is compared for some values of the advection coefficient a. In addition, some numerical results for different choices of t_{train} and N_{POD} are shown and some conclusions are drawn. Finally, the CPU times required by the CT-FOM and CT-ROM are compared, showing that the latter generates a similar approximation with a lower computational cost.

The Péclet number is used to consider a range of advection-diffusion problems. It is defined to be the ratio of the advection to the diffusion transport

$$Pe = \frac{a\Delta x}{\nu},$$

and, depending on the value of this number, the problem is advection or diffusion dominated. In the numerical experiments, the value of the diffusion coefficient is fixed with $\nu = 0.001$, the cell size is $\Delta x = 0.01$ and the advection coefficient a takes the values shown in Table 1. The corresponding Péclet numbers are also given in this table.

a	0.005	0.025	0.05	0.1	0.15	0.2	0.25	0.3	0.35	0.4	0.45	0.5
Pe	0.05	0.25	0.5	1	1.5	2	2.5	3	3.5	4	4.5	5

Table 1: Case 1: Values of the advection coefficient and the Péclet number.

The application of the CT-ROM to this problem is now described. The starting point of the characteristic curve $d(t)$ is placed at the location of the maximum of the initial Gaussian function, i.e., $d(0) = 1$. In Figure 2, the mesh and the characteristic curve (11) for $a = 0.5$ in the physical domain are shown.

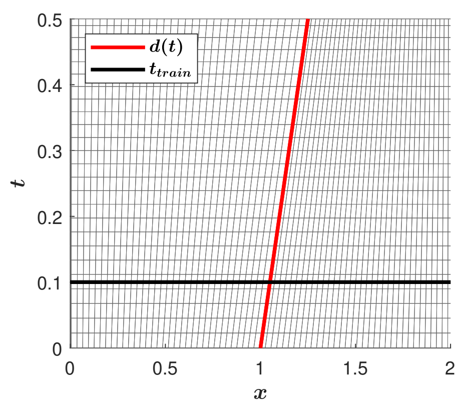

Figure 2: Case 1: Time evolution of the physical mesh.

The spatial domain $[0, 2]$ is divided into $N_x = 200$ volume cells, so that the cell size in the transformed domain is $\Delta\tilde{x} = 0.01$. The time step is computed to satisfy the following stability condition

$$\Delta t = CFL \frac{\Delta\tilde{x}^2}{\Delta\tilde{x}\max\{\tilde{a}_1, \tilde{a}_2\} + 2\max\{\tilde{\nu}_1, \tilde{\nu}_2\}}, \tag{16}$$

where the modified velocities and modified viscosities are

$$\begin{aligned}
\tilde{a}_1 &= \max_{0\le\tilde{x}\le d(0)} \left| a\frac{d(0)}{d(t)} - a\frac{\tilde{x}}{d(t)} \right| = |a|\frac{d(0)}{d(t)}, \\
\tilde{a}_2 &= \max_{d(0)\le\tilde{x}\le L} \left| a\frac{L-d(0)}{L-d(t)} - a\frac{L-\tilde{x}}{L-d(t)} \right| = |a|\frac{L-d(0)}{L-d(t)}, \\
\tilde{\nu}_1 &= \nu\left(\frac{d(0)}{d(t)}\right)^2, \quad \tilde{\nu}_2 = \nu\left(\frac{L-d(0)}{L-d(t)}\right)^2.
\end{aligned}$$

To assess the predictive capability of ROM and CT-ROM, numerical solutions are computed with the FOM and CT-FOM up to $t_{train} = 0.1$ and approximations up to the final time $T = 0.5$ are obtained using the ROM and CT-ROM (see Figure 2 for the latter method). Unless otherwise stated, the number of modes in all the experiments performed in this case is $N_{POD} = 14$.

Lets first consider Case 1 with $a = 0.15$ and $a = 0.5$. The corresponding Péclet numbers are $Pe = 1.5$ and $Pe = 5$, and they are representative examples of diffusion dominated and advection dominated problems, respectively. In Figure 3, the IC and the computed solutions with both methods at $t_{train} = 0.1$ and $T = 0.5$ are shown. A separately computed FOM/CT-FOM solution at $T = 0.5$ is also included for comparison with the ROM/CT-ROM solutions.

Figure 4 illustrates how the CT-ROM works: i) the reduced order model is solved in the transformed mesh, so that the Gaussian profile of the IC remains fixed at the initial position and hardly changes (the decrease in amplitude is due to the given diffusion $\nu = 0.001$), this can be seen in Figure 4a; and ii) the inverse coordinate transformation is performed to recover the solution in the physical mesh at each time step. This implies that the initial Gaussian profile is transported in space due to the evolution of the mesh itself, as can be seen in Figure 4b.

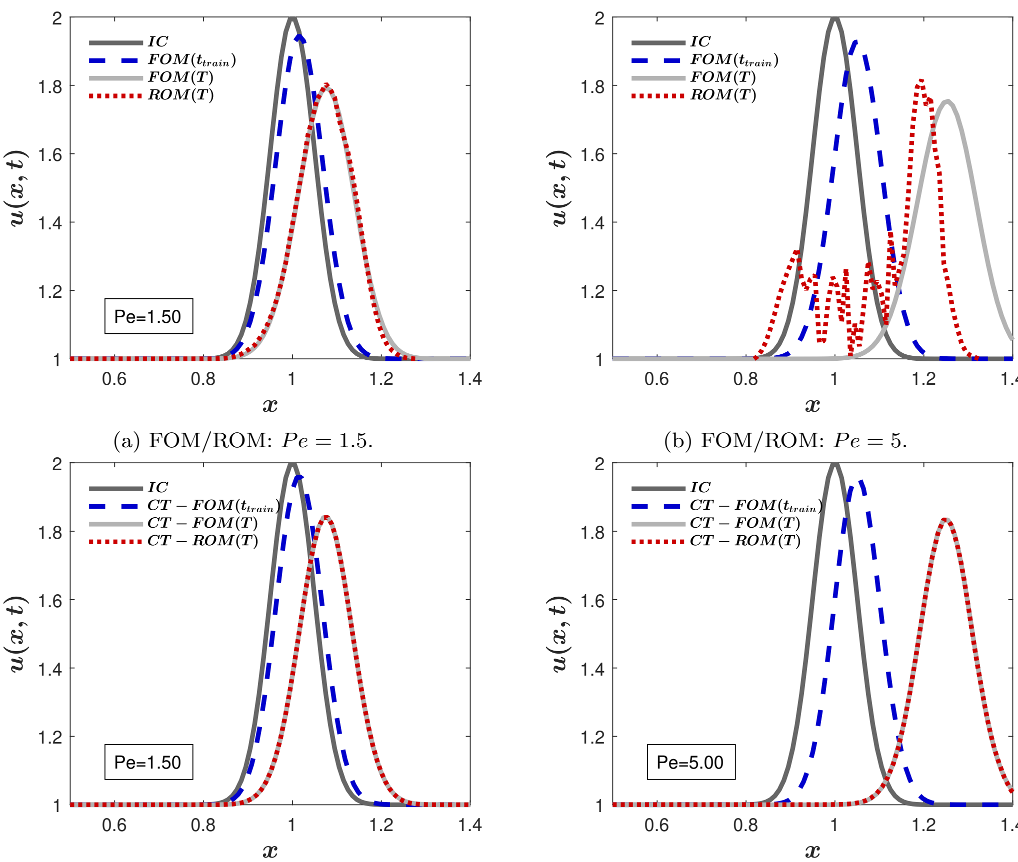

(a) FOM/ROM: $Pe = 1.5$.

(b) FOM/ROM: $Pe = 5$.

(c) CT-FOM/CT-ROM: $Pe = 1.5$.

(d) CT-FOM/CT-ROM: $Pe = 5$.

Figure 3: Case 1: Solutions computed with the FOM/ROM (top) and with the CT-FOM/CT-ROM (bottom).

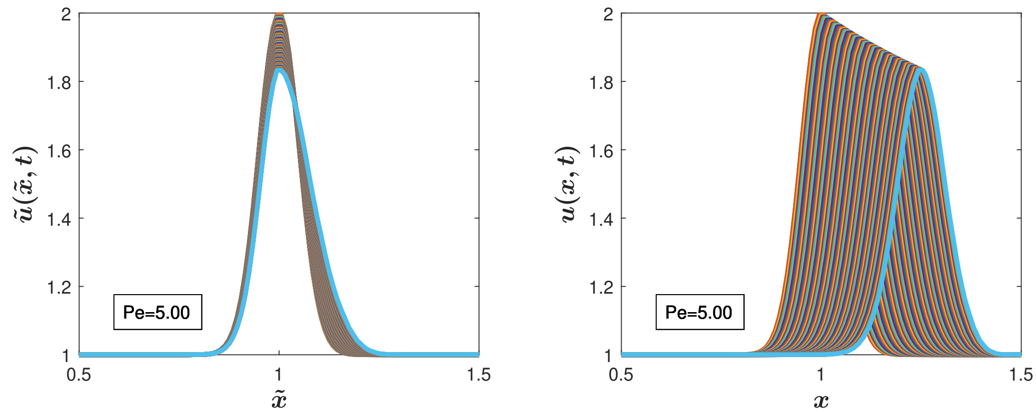

(a) Computational domain.

(b) Physical domain.

Figure 4: Case 1: Solutions computed with the CT-ROM on the computational and physical domains.

On the one hand, it can be seen from Figure 3a that, in the case of $Pe = 1.5$, ROM is able to predict the solution at times greater than the training time $t_{train} = 0.1$, whereas it is not possible for $Pe = 5$ as shown in Figure 3b. On the other hand, the CT-ROM is able to predict in time both examples; see Figures 3c and 3d. The ROM and the CT-ROM are compared in detail by calculating at all time levels t^n

$$D_S^n = \frac{\|\mathbf{u}^n - \mathbf{v}^n\|_{\ell^2}}{\|\mathbf{u}^n\|_{\ell^2}}, \quad D_{CT}^n = \frac{\|\tilde{\mathbf{u}}^n - \mathbf{w}^n\|_{\ell^2}}{\|\tilde{\mathbf{u}}^n\|_{\ell^2}},$$

where $\|\cdot\|_{\ell^2}$ is the standard discrete $L^2([0, L])$ norm for mesh functions. These differences are shown in Figure 5 and it is observed that the CT-ROM does indeed allow to predict in time with high accuracy for the set of problems considered including both advection-dominated and diffusion-dominated problems.

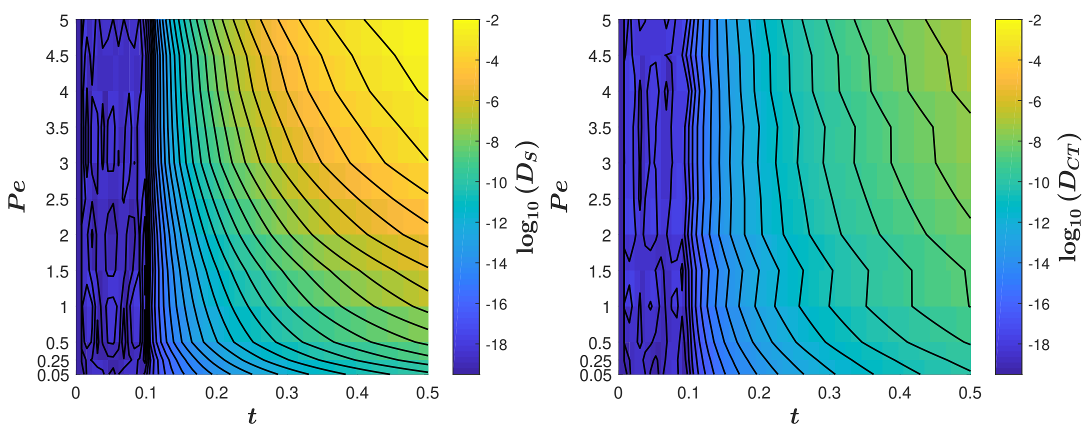

(a) ROM: $\log_{10}$ of the difference D_S.

(b) CT-ROM: $\log_{10}$ of the difference D_{CT}.

Figure 5: Case 1: Differences D_S and D_{CT}.

In Figure 6, the differences D_S^n and D_{CT}^n are shown for four different values of $Pe = 0.05, 1.5, 3, 5$, whose advective velocities are $a = 0.005, 0.15, 0.3, 0.5$, respectively. On the one hand, it can be seen that, for the most advection-dominated problem, the improvement is more significant and D_{CT}^n is reduced by five orders of magnitude with respect to D_S^n. On the other hand, D_{CT}^n and D_{CT}^n have similar orders of magnitude at all time levels when the problem is diffusion-dominated.

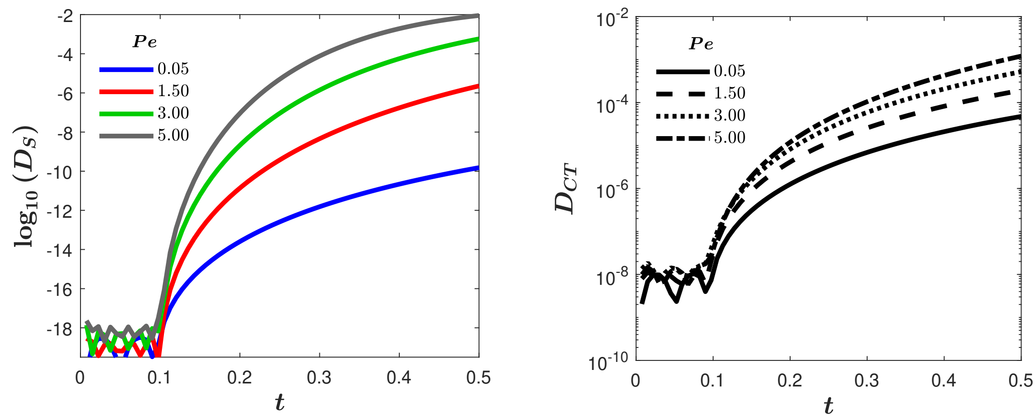

(a) ROM: $\log_{10}$ of the difference D_S.

(b) CT-ROM: $\log_{10}$ of the difference D_{CT}.

Figure 6: Case 1: Sections of differences D_S and D_{CT}.

The Péclet numbers shown in Figures 5b and 6b are only used as a tool to compare the results with those in Figures 5a and 6a, respectively. In the new coordinate system, (13) leads to the definition of a modified Péclet number

$$\tilde{Pe} = \begin{cases} \dfrac{a\dfrac{d(0)-\tilde{x}}{d(t)}}{\nu\left(\dfrac{d(0)}{d(t)}\right)^2}\Delta\tilde{x} = Pe\dfrac{d(0)-\tilde{x}}{d(0)}, & \text{if } 0 \leq \tilde{x} \leq d(0), \\ \dfrac{a\dfrac{\tilde{x}-d(0)}{L-d(t)}}{\nu\left(\dfrac{L-d(0)}{L-d(t)}\right)^2}\Delta\tilde{x} = Pe\dfrac{\tilde{x}-d(0)}{L-d(0)}, & \text{if } d(0) < \tilde{x} \leq L. \end{cases}$$

Thus, this modified Péclet number depends on the variable $\tilde{x}$, i.e., $\tilde{Pe} = \tilde{Pe}(\tilde{x})$, and it is a piecewise linear function with $\tilde{Pe}(0) = \tilde{Pe}(L) = 1$ and $\tilde{Pe}(d(0)) = 0$. Therefore, $\tilde{Pe}(\tilde{x}) \leq Pe$ for all $\tilde{x} \in [0, L]$ and these numbers are only the same at the endpoints of the domain $\tilde{x} = 0, L$.

To analyze the influence of the training time t_{train} on the accuracy of the computed solution with the CT-ROM, a series of results have been computed by varying the ratio between the number of cells and the training time. Table 2 shows the difference $D_{CT}^{N_T}$ of the results of the CT-ROM at the final time $T = 0.5$ with respect to the reference solution computed with the CT-FOM. These results have been obtained for three different mesh refinements, $N_x = 100$, 200 and 400, and for three different training times, $t_{train} = 0.05$, 0.1 and 0.2. This table shows that the differences $D_{CT}^{N_T}$ are small in all the cases, but they grow by an order of magnitude from $t_{train} = 0.2$ to $t_{train} = 0.05$. In addition, for different mesh refinements, the value of $D_{CT}^{N_T}$ remains in the same order of magnitude.

t_{train}/N_x	100	200	400
0.2	$1.62 \cdot 10^{-4}$	$1.70 \cdot 10^{-4}$	$2.01 \cdot 10^{-4}$
0.1	$1.28 \cdot 10^{-3}$	$1.19 \cdot 10^{-3}$	$9.74 \cdot 10^{-4}$
0.05	$2.94 \cdot 10^{-3}$	$3.30 \cdot 10^{-3}$	$4.00 \cdot 10^{-3}$

Table 2: Case 1: Differences $D_{CT}^{N_T}$ vs. the training time for three different mesh refinements.

By setting $N_x = 200$ and $t_{train} = 0.1$, the influence of the number of modes N_{POD} used by the CT-ROM is next analysed. In this case, $N_{train} = 15$ and $N_{POD} = 3, 5, 7, 10$ and 15. The numerical results are given in Table 3, where it can be observed that the larger N_{POD} is, the smaller the differences $D_{CT}^{N_T}$ are, although the order of magnitude remains constant. It is important to note that the CT-FOM and the CT-ROM give similar approximations to the solution even for a small number of modes.

N_{POD}	3	5	7	10	15
$D_{CT}^{N_T}$	$5.09 \cdot 10^{-3}$	$2.34 \cdot 10^{-3}$	$1.64 \cdot 10^{-3}$	$1.31 \cdot 10^{-3}$	$1.19 \cdot 10^{-3}$

Table 3: Case 1: Differences $D_{CT}^{N_T}$ with $N_x = 200$ volume cells, $t_{train} = 0.1$ and some values of N_{POD}.

To check the efficiency gain of the CT-ROM vs. the CT-FOM, the CPU times of Case 1 with $a = 0.5$ are plotted in Figure 7, where $N_x = 100$, 200, 500, 1000, 2000 and 3000, $t_{train} = 0.1$ and $T = 0.5$. The CPU times of the CT-ROM at $T = 0.5$ are lower than those of CT-FOM for the same final time. The CPU times required by the CT-FOM to generate the training solutions have been added to the figure so that it can be seen that, with $t_{train} = 0.1$, they are similar to those of the CT-ROM up to $T = 0.5$.

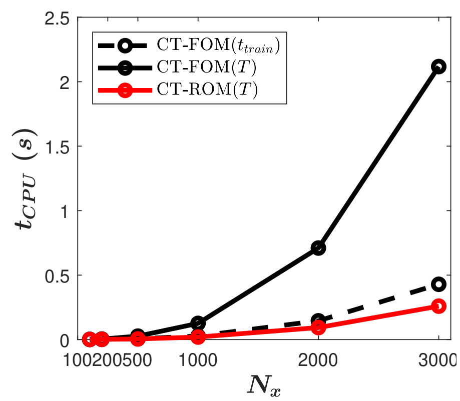

Figure 7: Case 1: CPU times measurement of the CT-FOM and the CT-ROM.

Case 2. 1D transport of Gaussian IC with $a = a(t)$

Case 2 considers the 1D linear equation

$$\frac{\partial u(x,t)}{\partial t} + a\frac{\partial u(x,t)}{\partial x} = 0, \quad (x,t) \in (0,2) \times (0,2],$$

with time-dependent advective velocity $a(t) = 1 - t$. The Gaussian IC (9) and periodic BC (10) are considered. The starting point of the characteristic curve is placed at the point $d(0) = 1$ where the Gaussian IC reaches its maximum value.

The spatial domain $[0,2]$ is divided into $N_x = 200$ volume cells, so that the cell size is $\Delta\tilde{x} = 0.01$. The CFL number considered in this case is 0.9 and the time step is computed to satisfy stability condition (16). Solutions are computed with the CT-FOM (14) up to $t_{train} = 0.1$ and approximate solutions are computed using the CT-ROM (15) up to $T = 2$. In this case, $N_{train} = 10$ and the number of modes is $N_{POD} = 10$. The physical mesh evolves as shown in Figure 8 where the characteristic curve is $d(t) = 1 + t - t^2/2$.

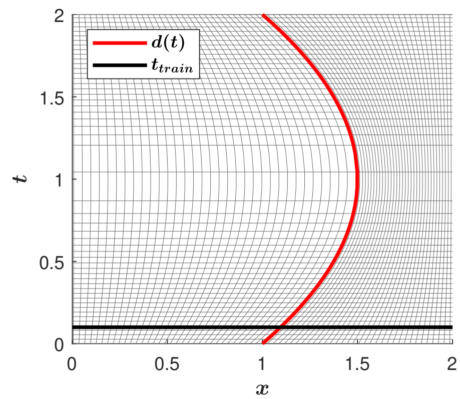

Figure 8: Case 2: Time evolution of the physical mesh.

This case has been designed in such a way that the Gaussian IC moves to the right until $t = 1$, when $a = 0$, and, from that moment on, it moves to the left. Finally, at $T = 2$, the solution arrives at the initial position. As shown in Figure 9, the CT-ROM is able to reproduce the change of direction in the movement of the solution with a training time much shorter than the time in which the velocity changes sign, i.e., $t_{train} = 0.1 < 1$. The CT-ROM solution at the final time $T = 2$ reproduces accurately the reference solution computed with the CT-FOM.

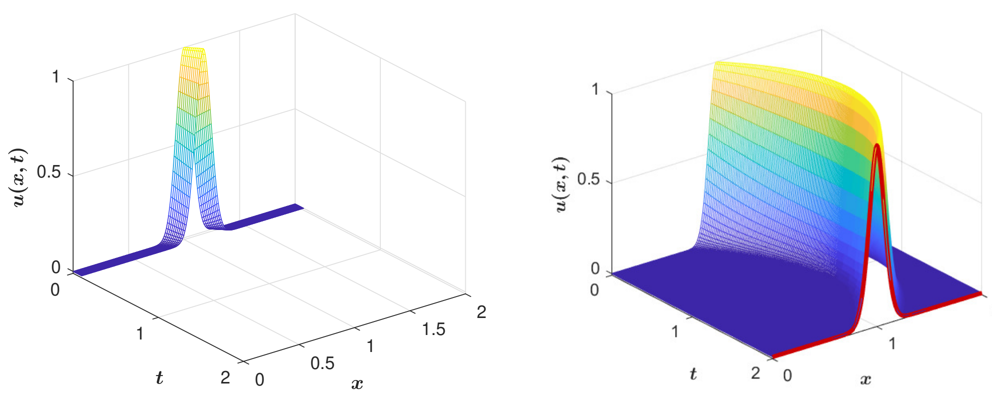

(a) CT-FOM.

(b) CT-ROM.

Figure 9: Case 2: Solutions computed with the CT-FOM and the CT-ROM.

Case 3. 1D reactive transport of two coupled functions

Consider the following system of equations that models the reactive transport of two coupled solutes $u(x,t)$ and $v(x,t)$

$$\begin{aligned} \frac{\partial u(x,t)}{\partial t} + a\frac{\partial u(x,t)}{\partial x} &= -cu(x,t), \\ \frac{\partial v(x,t)}{\partial t} + a\frac{\partial v(x,t)}{\partial x} &= cu(x,t), \end{aligned} \tag{17}$$

with $(x,t) \in (0,L) \times (0,T]$, $L = T = 10$, the value of the advective velocity is $a = 0.2$ and the reactive coefficient is $c = 0.1$. The following IC is considered

$$u(x,0) = \begin{cases} 0, & \text{if } 0 < x \leq 0.3, \\ \sin\left(\frac{2\pi}{L}(x-0.3)\right), & \text{if } 0.3 < x < 5.3, \\ 0, & \text{if } 5.3 \leq x < 10, \end{cases}$$
$$v(x,0) = \begin{cases} 1, & \text{if } 0 < x \leq 0.3, \\ 1-\sin\left(\frac{2\pi}{L}(x-0.3)\right), & \text{if } 0.3 < x < 5.3, \\ 1, & \text{if } 5.3 \leq x < 10, \end{cases}$$

and the BC

$$u(0,t) = u(L,t) = 0, \quad v(0,t) = v(L,t) = 1.$$

Using again the mapping (12), problem (17) is transformed in the following system of partial differential equations

$$\begin{cases} \dfrac{\partial \tilde{u}}{\partial t} + a\dfrac{d_u(0)-\tilde{x}}{d_u(t)}\dfrac{\partial \tilde{u}}{\partial \tilde{x}} = -c\tilde{u}, & \text{if } 0 < \tilde{x} \leq d_u(0), \\ \dfrac{\partial \tilde{u}}{\partial t} + a\dfrac{\tilde{x}-d_u(0)}{L-d_u(t)}\dfrac{\partial \tilde{u}}{\partial \tilde{x}} = -c\tilde{u}, & \text{if } d_u(0) < \tilde{x} < L, \\ \dfrac{\partial \tilde{v}}{\partial t} + a\dfrac{d_v(0)-\tilde{x}}{d_v(t)}\dfrac{\partial \tilde{v}}{\partial \tilde{x}} = c\tilde{u}, & \text{if } 0 < \tilde{x} \leq d_v(0), \\ \dfrac{\partial \tilde{v}}{\partial t} + a\dfrac{\tilde{x}-d_v(0)}{L-d_v(t)}\dfrac{\partial \tilde{v}}{\partial \tilde{x}} = c\tilde{u}, & \text{if } d_v(0) < \tilde{x} < L, \end{cases} \tag{18}$$

where $d_u(t)$ and $d_v(t)$ are the characteristic curves for each equation

$$d_u(t) = d_u(0) + at, \quad d_v(t) = d_v(0) + at,$$

passing through the points $(d_u(0), 0)$ and $(d_v(0), 0)$ with $d_u(0) = d_v(0) = 0.3$ in this case. The CT-FOM and the CT-ROM for the system of PDEs (18) are very similar to the ones deduced for Case 1 and they are not included here.

Regarding the data of the numerical problem, the spatial domain $[0, L = 10]$ is divided into $N_x = 100$ volume cells and then the spatial step size is $\Delta\tilde{x} = 0.1$. Additionally, CFL $= 0.9$, $t_{train} = 4$ with $N_{train} = 49$ and $N_{\text{POD}} = 14$.

Figure 10 shows the IC, the results of the CT-ROM at the final time $T = 10$ and the result of the CT-FOM at $t_{train} = 4$. A separately calculated CT-FOM solution at $T = 10$ is also included for comparison with the CT-ROM solution. The CT-ROM accurately predicts the location and the shape of the solution at the final time $T = 10$, although some small oscillations appear around the sinusoidal profile.

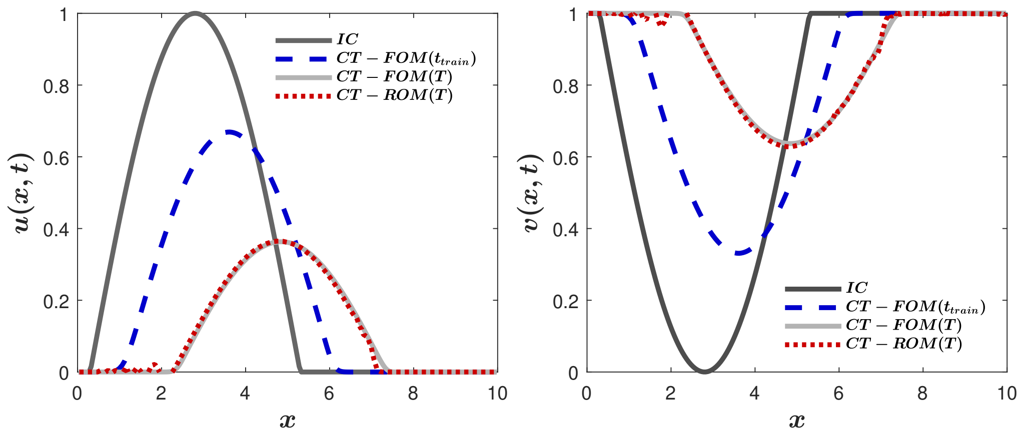

Figure 10: Case 3: Solutions computed with the CT-FOM and the CT-ROM.

Case 4. 1D transport of Gaussian IC with linearized SWE

Several hydraulic phenomena such as river systems can be simulated using the SWE, also known as depth-averaged St. Venant equations, to model the motion of water with a free surface [15]. These equations are obtained by integration of the three-dimensional Navier-Stokes equations over the depth, with the assumption of hydrostatic vertical pressure distribution, i.e., negligible vertical accelerations. The 1D linearized SWE are

$$\begin{aligned} \frac{\partial h(x,t)}{\partial t} + h_0 \frac{\partial u(x,t)}{\partial x} &= 0, \\ \frac{\partial u(x,t)}{\partial t} + g \frac{\partial h(x,t)}{\partial x} &= 0, \end{aligned} \tag{19}$$

where $h(x,t)$ is the water depth and $u(x,t)$ is the depth-averaged water velocity in the x-direction, h_0 is the undisturbed water depth at $t = 0$ and g is the gravitational acceleration.

In order to approximate problem (19) in a new coordinate system using the mapping (12), it is necessary to decouple the system of equations [8]. The procedure is explained below. First, problem (19) is written in vector form

$$\frac{\partial}{\partial t}\mathbf{U} + \mathbf{J}\frac{\partial}{\partial x}\mathbf{U} = 0, \tag{20}$$

where $\mathbf{U} = (h, u)^T$ is the conserved variables vector and

$$\mathbf{J} = \begin{pmatrix} 0 & h_0 \\ g & 0 \end{pmatrix}$$

is a diagonalizable Jacobian matrix with $\mathbf{J} = \mathbf{P}\boldsymbol{\Lambda}\mathbf{P}^{-1}$ and

$$\boldsymbol{\Lambda} = \begin{pmatrix} c & 0 \\ 0 & -c \end{pmatrix}, \quad \mathbf{P} = \begin{pmatrix} 1 & 1 \\ c/h_0 & -c/h_0 \end{pmatrix}, \quad c = \sqrt{gh_0}.$$

Second, the conserved variables are decoupled by multiplying (20) by $\mathbf{P}^{-1}$. Then,

$$\frac{\partial \mathbf{W}}{\partial t} + \boldsymbol{\Lambda}\frac{\partial \mathbf{W}}{\partial x} = 0, \tag{21}$$

where $\mathbf{W} = \mathbf{P}^{-1}\mathbf{U} = (\omega_1, \omega_2)^T$ are the characteristic variables

$$\omega_1 = (ch + h_0 u)/2c, \quad \omega_2 = (ch - h_0 u)/2c. \tag{22}$$

Finally, the mapping (12) is applied to problem (21) and the characteristic variables $\tilde{w}_i$ in the new coordinate system are separately approximated with a CT-FOM and a CT-ROM as in Case 1.

In this case, $h_0 = 1$, the spatial domain is $[0, L = 4]$ and the final time is $T = 0.4$. The IC are defined as

$$h(x,0) = 1 + e^{-200(x-2)^2}, \quad u(x,0) = 0, \quad 0 \le x \le L,$$

and periodic BC are considered

$$h(0,t) = h(L,t), \quad u(0,t) = u(L,t), \quad 0 < t \le T.$$

From (22), observe that the IC and BC of the characteristic variables are

$$w_i(x,0) = h/2,\ 0 \le x \le L, \quad w_i(0,t) = w_i(L,t),\ 0 < t \le T, \quad i = 1,2.$$

The characteristic curves for each decoupled equation are given by

$$d_1(t) = d_1(0) + ct, \quad d_2(t) = d_2(0) - ct, \quad 0 < t \le T,$$

with $d_1(0) = d_2(0) = 2$. Note that the functions $w_i(x,0)$ reach the maximum value at $d(0) = 2$.

Regarding the data of the numerical problem, the spatial domain $[0,4]$ is divided into $N_x = 200$ volume cells, so that the cell size is $\Delta\tilde{x} = 0.02$. In this case, CFL$= 0.9$, $t_{train} = 0.0625$, $N_{POD} = 5$ and $N_{train} = 5$ time levels are solved with the CT-FOM.

Figure 11 shows the IC, the results of the CT-FOM at $t_{train} = 0.0625$ and the results of the CT-ROM at $T = 0.4$. A separately calculated CT-FOM solution at $T = 0.4$ is also included for comparison with the CT-ROM solution. The CT-ROM is able to predict the position and the amplitude of the solution at the final time $T = 0.4$.

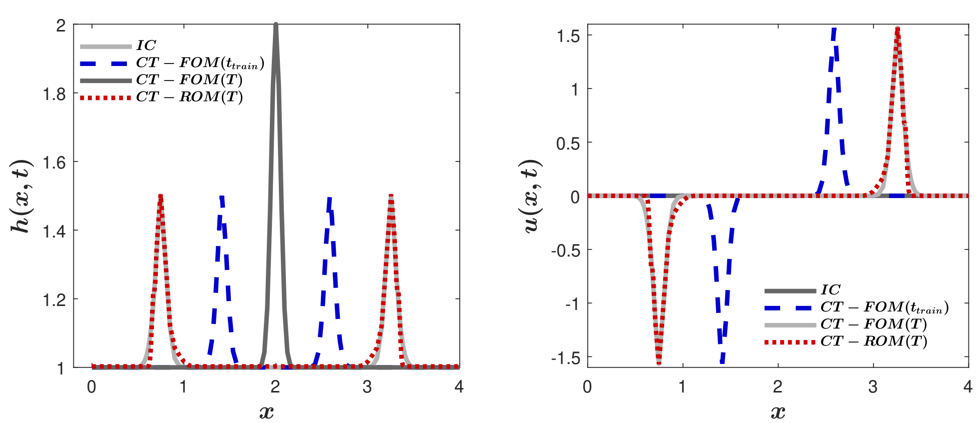

Figure 11: Case 4: Solutions computed with the CT-FOM and the CT-ROM.

The CPU times of Case 4 are plotted in Figure 12, where $N_x = 100$, 200, 500, 1000, 2000 and 3000. The CPU times of the CT-ROM at $T = 0.4$ are lower than those of

CT-FOM at the training time $t_{train} = 0.0625$ and therefore even lower than those at the final time.

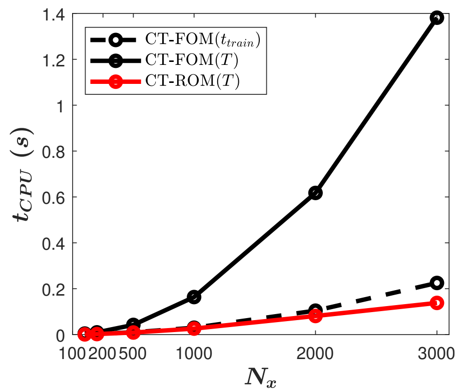

Figure 12: Case 4: CPU times measurement of CT-FOM and CT-ROM.

3.2. CT-ROM applied to 1D inviscid Burgers' equation

Consider the 1D inviscid Burgers' equation

$$\frac{\partial u(x,t)}{\partial t} + u(x,t)\frac{\partial u(x,t)}{\partial x} = 0, \ (x,t) \in (0,L) \times (0,T]\,. \tag{23}$$

The FOM to approximate the solution of this problem is based on the FV method

$$\frac{u_j^{n+1} - u_j^n}{\Delta t} + \frac{\delta f_{j+1/2}^{n,-,*} + \delta f_{j-1/2}^{n,+,*}}{\Delta x} = 0, \ j = 1, ..., N_x, \tag{24}$$

where the numerical flux differences are defined as in (3) and (4), with the following approximate wave celerity

$$\bar{\lambda}_{j+1/2}^n = \frac{f_{i+1}^n - f_i^n}{u_{j+1}^n - u_j^n} = \frac{1}{2}\frac{(u_{j+1}^n)^2 - (u_j^n)^2}{u_{j+1}^n - u_j^n} = \frac{1}{2}\left(u_{j+1}^n + u_j^n\right).$$

The explicit updating equation of the reduced order model is obtained following the same three steps indicated in Section 2 for the standard POD method, leading to

$$\hat{v}_p^{n+1} = \hat{v}_p^n - \frac{\Delta t}{\Delta x}\left(\hat{\mathbf{v}}^n\right)^T A^{(p)}\hat{\mathbf{v}}^n + \frac{\Delta t}{\Delta x}\left|\hat{\mathbf{v}}^n\right|^T B^{(p)}\hat{\mathbf{v}}^n, \tag{25}$$

where

$$\begin{aligned}
A_{qk}^{(p)} &= \Lambda_{qk;p}^1 + \sum_{j=2}^{N_x-1} \frac{1}{4}\left[\left(\phi_{j+1,k} + \phi_{j,k}\right)\left(\phi_{j+1,q} - \phi_{j,q}\right) + \left(\phi_{j,k} + \phi_{j-1,k}\right)\left(\phi_{j,q} - \phi_{j-1,q}\right)\right]\phi_{j,p} \\
&\quad + \Lambda_{qk;p}^{N_x}, \\
B_{qk}^{(p)} &= \beta_{qk;p}^1 + \sum_{j=2}^{N_x-1} \frac{1}{4}\left[\left|\phi_{j+1,k} + \phi_{j,k}\right|\left(\phi_{j+1,q} - \phi_{j,q}\right) - \left|\phi_{j,k} + \phi_{j-1,k}\right|\left(\phi_{j,q} - \phi_{j-1,q}\right)\right]\phi_{j,p} \\
&\quad + \beta_{qk;p}^{N_x}.
\end{aligned}$$

For a full development of the procedure to obtain the ROMs, see [48]. The terms $\Lambda_{qk;p}^1$, $\Lambda_{qk;p}^{N_x}$, $\beta_{qk;p}^1$ and $\beta_{qk;p}^{N_x}$ are obtained following the same procedure as in (7) and (8).

In Cases 5, 6 and 7 considered in this section, the standard ROM (25), although it is trained until the final time (i.e., $t_{train} = T$), is not able to accurately reproduce the shock and rarefaction wave solutions, due to the appearance of oscillations, as can be seen below. However, a ROM based on a coordinate transformation using only two sub-domains in the computational domain may not be able to reproduce the generation of shocks or rarefactions. This drawback is overcome by considering more sub-domains separated by characteristic curves which are appropriately chosen. The transformation when two characteristic curves are required is explained below, and it is similarly defined in the general case. In particular, the ICs in Cases 5 and 6 described below are piecewise linear functions in the intervals $[0, d_1(0)], [d_1(0), d_2(0)]$ and $[d_2(0), L]$; it is a decreasing linear function on $[d_1(0), d_2(0)]$ generating a shock in Case 5 whereas it is increasing in Case 6 and its solution becomes a rarefaction wave. This kind of ICs are considered below, except in Case 7 where a polynomial (but not linear) piecewise IC is imposed.

Let the characteristic curves be

$$d_i'(t) = u(d_i(t), t), \quad d_i(0) \text{ given}, \ i = 1, 2, \quad 0 \le t \le t_c,$$

where $t_c \le T$ is the critical value such that the solution is single-valued and $d_1(t) \le d_2(t)$ is assumed for $0 \le t \le t_c$. If the two characteristic curves intersect, $d_1(t_c) = d_2(t_c)$, then a shock wave is generated at $t = t_c$ and a similar transformation to (12) is used for $t > t_c$. If a rarefaction wave is produced by the Burger's equation, three sub-domains are considered for $0 \le t \le T$.

When the spatial domain is divided into three sub-domains, the coordinate transformation for the characteristic curves $d_1(t)$ and $d_2(t)$, reads as follows

$$\tilde{x}(t) = \begin{cases} \dfrac{d_1(0)}{d_1(t)} x, & \text{if } 0 \le x < d_1(t), \\ d_1(0) + \dfrac{d_2(0) - d_1(0)}{d_2(t) - d_1(t)} (x - d_1(t)), & \text{if } d_1(t) \le x \le d_2(t), \\ L - \dfrac{L - d_2(0)}{L - d_2(t)} (L - x), & \text{if } d_2(t) < x \le L. \end{cases}$$

The 1D Burgers' equation (23) in the transformed domain is

$$\begin{cases} \dfrac{\partial \tilde{u}}{\partial t} + \left(\tilde{u}(\tilde{x}, t) \dfrac{d_1(0)}{d_1(t)} - \tilde{u}(d_1(0), t) \dfrac{\tilde{x}}{d_1(t)} \right) \dfrac{\partial \tilde{u}}{\partial \tilde{x}} = 0, & \text{if } 0 < \tilde{x} < d_1(0), \\ \dfrac{\partial \tilde{u}}{\partial t} = 0, & \text{if } d_1(0) \le \tilde{x} \le d_2(0), \\ \dfrac{\partial \tilde{u}}{\partial t} + \left(\tilde{u}(\tilde{x}, t) \dfrac{L - d_2(0)}{L - d_2(t)} - \tilde{u}(d_2(0), t) \dfrac{L - \tilde{x}}{L - d_2(t)} \right) \dfrac{\partial \tilde{u}}{\partial \tilde{x}} = 0, & \text{if } d_2(0) < \tilde{x} < L, \end{cases}$$

where $\tilde{u}(\tilde{x}, t) = u(x, t)$. The CT-FOM of the 1D inviscid Burgers' equation is obtained by means of the FV method [28, 30, 33]

$$\begin{aligned} \tilde{u}_j^{n+1} &= \tilde{u}_j^n - \frac{\Delta t}{\Delta \tilde{x}} \left[\frac{d_1^0}{d_1^n} \left(\delta \tilde{f}_{j+1/2}^{n,-,*} + \delta \tilde{f}_{j-1/2}^{n,+,*} \right) - \frac{\tilde{u}_{J_1+1/2}^n}{d_1^n} \left(\delta \tilde{f}_{j+1/2}^{n,-,**} + \delta \tilde{f}_{j-1/2}^{n,+,**} \right) \right], \\ & \qquad \text{if } 0 < \tilde{x}_j < d_1^0, \\ \tilde{u}_j^{n+1} &= \tilde{u}_j^n, \qquad \text{if } d_1^0 \le \tilde{x}_j \le d_2^0, \\ \tilde{u}_j^{n+1} &= \tilde{u}_j^n - \frac{\Delta t}{\Delta \tilde{x}} \left[\frac{L - d_2^0}{L - d_2^n} \left(\delta \tilde{f}_{j+1/2}^{n,-,*} + \delta \tilde{f}_{j-1/2}^{n,+,*} \right) - \frac{\tilde{u}_{J_2+1/2}^n}{L - d_2^n} \left(\delta \tilde{f}_{j+1/2}^{n,-,**} + \delta \tilde{f}_{j-1/2}^{n,+,**} \right) \right], \\ & \qquad \text{if } d_2^0 < \tilde{x}_j < L, \end{aligned} \tag{26}$$

where $\tilde{x}_{J_1+1/2} = d_1^0$ and $\tilde{x}_{J_2+1/2} = d_2^0$; the numerical fluxes are

$$\delta \tilde{f}^{n,\pm,*}_{j+1/2} = \bar{\lambda}^{n,\pm,*}_{j+1/2} \delta \tilde{u}^n_{j+1/2}, \quad \delta \tilde{f}^{n,\pm,**}_{j+1/2} = \bar{\lambda}^{n,\pm,**}_{j+1/2} \delta \tilde{u}^n_{j+1/2},$$

with $\delta \tilde{u}^n_{j+1/2} = \tilde{u}^n_{j+1} - \tilde{u}^n_j$; and

$$\begin{aligned}
\bar{\lambda}^{n,\pm,*}_{j+1/2} &= \frac{1}{2}\left(\bar{\lambda}^{n,*}_{j+1/2} \pm \left|\bar{\lambda}^{n,*}_{j+1/2}\right|\right) = \frac{1}{4}\left(\tilde{u}^n_{j+1} + \tilde{u}^n_j \pm \left|\tilde{u}^n_{j+1} + \tilde{u}^n_j\right|\right), \\
\bar{\lambda}^{n,+,**}_{j+1/2} &= \frac{1}{2}\left(\bar{\lambda}^{n,**}_{j+1/2} + \left|\bar{\lambda}^{n,**}_{j+1/2}\right|\right) = \begin{cases} \tilde{x}_{j+1/2}, & \text{if } \tilde{x}_j \le d_1^0, \\ 0, & \text{if } d_1^0 \le \tilde{x}_j \le d_2^0, \\ L - \tilde{x}_{j+1/2}, & \text{if } d_2^0 \le \tilde{x}_j, \end{cases} \\
\bar{\lambda}^{n,-,**}_{j+1/2} &= \frac{1}{2}\left(\bar{\lambda}^{n,**}_{j+1/2} - \left|\bar{\lambda}^{n,**}_{j+1/2}\right|\right) = 0.
\end{aligned}$$

In scheme (26), the characteristic curves are approximated with the explicit Euler method

$$\frac{d_i^{n+1} - d_i^n}{\Delta t} = (\tilde{u}_i)^n_{J_i+1/2}, \; i = 1, 2.$$

The intrusive CT-ROM is obtained from the CT-FOM (26) as has been done in previous cases

$$\begin{aligned}
\hat{v}^{n+1}_p = \hat{v}^n_p &- \frac{\Delta t}{\Delta \tilde{x}} \frac{d_0}{d(t)} \left[(\hat{\mathbf{v}}^n)^T \left(A^L\right)^{(p)} \hat{\mathbf{v}}^n - |\hat{\mathbf{v}}^n|^T \left(B^L\right)^{(p)} \hat{\mathbf{v}}^n\right] + \frac{\Delta t}{\Delta \tilde{x}} \frac{1}{d(t)} C^L \hat{\mathbf{v}}^n \\
&- \frac{\Delta t}{\Delta \tilde{x}} \frac{L - d_0}{L - d(t)} \left[(\hat{\mathbf{v}}^n)^T \left(A^R\right)^{(p)} \hat{\mathbf{v}}^n - |\hat{\mathbf{v}}^n|^T \left(B^R\right)^{(p)} \hat{\mathbf{v}}^n\right] + \frac{\Delta t}{\Delta \tilde{x}} \frac{1}{L - d(t)} C^R \hat{\mathbf{v}}^n, \quad (27)
\end{aligned}$$

with the following matrices

$$\begin{aligned}
\left(A^L\right)^{(p)}_{qk} &= \Lambda^1_{qk;p} + \frac{1}{4} \sum_{j=2}^{J_1} \left[\left(\phi_{j+1,k} + \phi_{j,k}\right)\left(\phi_{j+1,q} - \phi_{j,q}\right) + \left(\phi_{j,k} + \phi_{j-1,k}\right)\left(\phi_{j,q} - \phi_{j-1,q}\right)\right] \phi_{j,p}, \\
\left(B^L\right)^{(p)}_{qk} &= \beta^1_{qk;p} + \frac{1}{4} \sum_{j=2}^{J_1} \left[\left|\phi_{j+1,k} + \phi_{j,k}\right|\left(\phi_{j+1,q} - \phi_{j,q}\right) - \left|\phi_{j,k} + \phi_{j-1,k}\right|\left(\phi_{j,q} - \phi_{j-1,q}\right)\right] \phi_{j,p}, \\
C^L_{kp} &= \zeta^1_{kp} + \frac{1}{4}\left(\phi_{J_1,k} + \phi_{J_1+1,k}\right) \sum_{j=2}^{J_1} \left(\tilde{x}_j + \tilde{x}_{j-1}\right)\left(\phi_{j,k} - \phi_{j-1,k}\right) \phi_{j,p}, \\
C^R_{kp} &= \frac{1}{4}\left(\phi_{J_2,k} + \phi_{J_2+1,k}\right) \sum_{j=J_2+1}^{N_x-1} \left(2L - \tilde{x}_j - \tilde{x}_{j-1}\right)\left(\phi_{j,k} - \phi_{j-1,k}\right) \phi_{j,p} + \zeta^{N_x}_{kp},
\end{aligned}$$

and the terms $\Lambda^1_{qk;p}$, $\beta^1_{qk;p}$, ζ^1_{kp} and $\zeta^{N_x}_{kp}$ can be computed following the same procedure as in (7) and (8) for Dirichlet and periodic BC, respectively. The matrices $(A^R)^{(p)}$ and $(B^R)^{(p)}$ are defined similarly to $(A^L)^{(p)}$ and $(B^L)^{(p)}$ and their limits of the summations are from $j = J_2 + 1$ to $N_x - 1$.

Case 5. 1D shock generation

In this Case 5, the generation of a shock wave is considered. The IC of this problem is

$$u(x, 0) = \begin{cases} 3, & \text{if } 0 < x \le d_1(0), \\ 3 - 2\dfrac{x - d_1(0)}{d_2(0) - d_1(0)}, & \text{if } d_1(0) < x < d_2(0), \\ 1, & \text{if } d_2(0) \le x \le L, \end{cases} \quad (28)$$

where $L = 2$ and the starting points of the characteristic curves are $d_1(0) = 0.25$ and $d_2(0) = 0.55$. A fixed boundary condition at $x = 0$ is considered

$$u(0,t) = 3, \quad 0 \leq t \leq T,$$

where the final time is $T = 0.65$ and the training time is $t_{train} = 0.35$.

The linear slope of the ramp in the IC (28) in the central sub-domain of the transformed coordinates will steepen until a shock is generated. At this time t_c, the two characteristic curves $d_1(t)$ and $d_2(t)$ converge into a single characteristic curve $d_3(t)$. All the points of the physical mesh in the central sub-domain are eventually mapped in the shock front and are no longer useful. Thus, the central sub-domain is suppressed to return to a two sub-domain problem. Numerically, at the critical time t_c, the problem is redefined by re-meshing, maintaining the original number of cells. The characteristic curves in the spatial domain are shown in Figure 13, where the time evolution of the physical mesh is represented for both the CT-FOM and the CT-ROM.

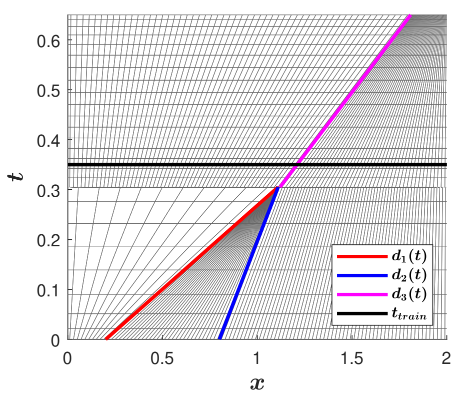

Figure 13: Case 5: Time evolution of the physical mesh for a shock wave generation.

The training time t_{train} is also shown in Figure 13 and it is observed that $t_{train} > t_c$ in this case. It should be noted that t_{train} could be shorter than t_c, but, in that case, it would be necessary to train the reduced order model with the CT-FOM before and after the shock wave is generated.

Before commenting on the results obtained with the CT-ROM for this case, it is necessary to take into account a couple of numerical considerations for solving a problem with three sub-domains. On the one hand, the confluence must be carefully solved, fitting the time step Δt to the critical time t_c satisfying that $d_1(t_c) = d_2(t_c)$, as depicted in Figure 14a. On the other hand, the starting point of the new characteristic curve $d_3(t_c)$ has to be moved to the nearest wall so that $\tilde{x}_{J+1/2} = d_3(t_c)$, in order to keep the stability, as depicted in Figure 14b. The coordinate transform method is very sensitive to this point.

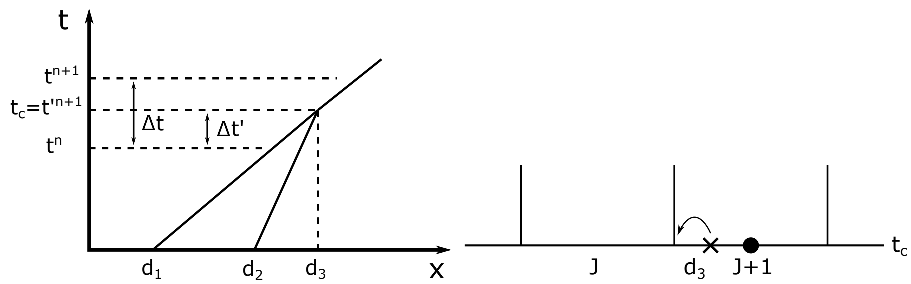

(a) Confluence of $d_1(t)$ and $d_2(t)$ into $d_3(t)$. (b) Moving $d_3(t)$ to the nearest interface.

Figure 14: Case 5: Numerical considerations for solving a problem with three sub-domains.

Regarding the data of the numerical problem, the spatial domain $[0, L = 2]$ is divided into $N_x = 100$ volume cells, so that $\Delta\tilde{x} = 0.02$. The CFL number considered is 0.9 and the time step is computed to satisfy the following stability condition

$$\Delta t = CFL \frac{\Delta \tilde{x}}{\max\{\tilde{a}_1, \tilde{a}_2\}},$$

where the modified velocities are

$$\begin{aligned}
\tilde{a}_1 &= \max_{0<\tilde{x}<d_1(0)} \left| \tilde{u}(\tilde{x}, t)\frac{d_1(0)}{d_1(t)} - \tilde{u}(d_1(0), t)\frac{\tilde{x}}{d_1(t)} \right|, \\
\tilde{a}_2 &= \max_{d_2(0)<\tilde{x}<L} \left| \tilde{u}(\tilde{x}, t)\frac{L - d_2(0)}{L - d_2(t)} - \tilde{u}(d_2(0), t)\frac{L - \tilde{x}}{L - d_2(t)} \right|.
\end{aligned}$$

The number of time steps used to train the CT-ROM is $N_{train} = 33$ and $N_{\text{POD}} = 10$.

Figure 15 shows the solutions computed with the FOM (24) and the ROM (25); and the CT-FOM (26) and the CT-ROM (27). From this figure, the following conclusions can be drawn: i) a proper prediction in time is computed with the CT-ROM; and ii) the solution computed with the CT-ROM does not exhibit spurious oscillations, as is the case with the ROM.

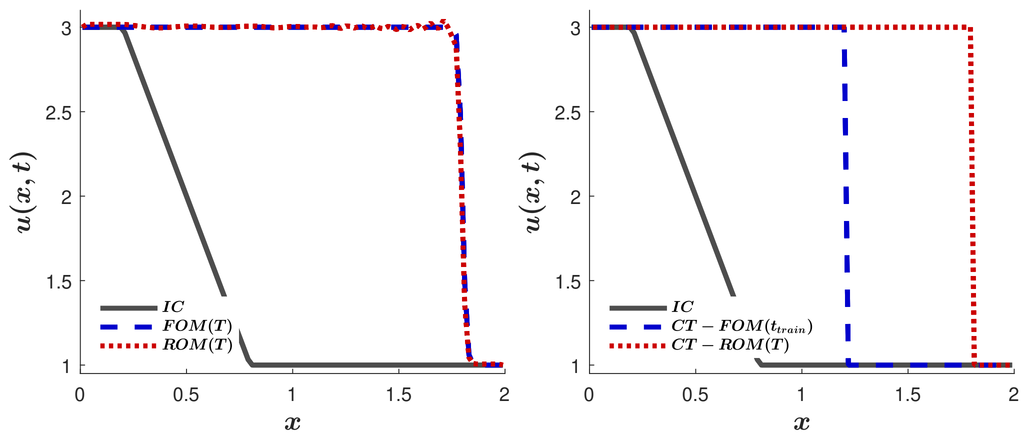

(a) FOM/ROM. (b) CT-FOM/CT-ROM.

Figure 15: Case 5: Solutions computed with the FOM/ROM (left) and with the CT-FOM/CT-ROM (right).

Cases 6 and 7. 1D rarefaction generation

Case 6 considers the Burger's equation (23) with the following IC

$$u(x,0) = \begin{cases} 1, & \text{if } 0 < x \le d_1(0), \\ 1 + 2\dfrac{x - d_1(0)}{d_2(0) - d_1(0)}, & \text{if } d_1(0) < x < d_2(0), \\ 3, & \text{if } d_2(0) \le x \le L, \end{cases}$$

where the spatial domain $[0, L = 2]$ is divided into $N_x = 100$ volume cells, the starting points of the characteristic curves are $d_1(0) = 0.2$ and $d_2(0) = 0.22$ and a fixed BC at $x = 0$ is considered

$$u(0,t) = 1, \quad 0 \le t \le T,$$

and the final time is $T = 0.5$. In this case, the characteristic curves d_1 and d_2 do not intersect. However, the starting points of the characteristic curves are so close to each other that a uniform mesh would contain very few points between them, and it could even contain only one point if it is coarse enough. Then, a finer mesh is set in the middle section, between $d_1(0)$ and $d_2(0)$, to properly reproduce the non-linear character of the Burgers' equation. Taking the latter into account, the spatial domain $[0, L]$ is divided into

$$[0, L] = [0, d_1(0)] \cup [d_1(0), d_2(0)] \cup [d_2(0), L],$$

and a piecewise uniform mesh is constructed with mesh widths $\Delta\tilde{x} = 0.02$, $\Delta\tilde{x} = 0.001$ and $\Delta\tilde{x} = 0.02$, respectively.

The CFL number considered is 0.9, the training time is $t_{train} = 0.2$, which corresponds to $N_{train} = 41$, and $N_{\text{POD}} = 11$. The time evolution of the physical mesh for both CT-FOM and CT-ROM is shown in Figure 16.

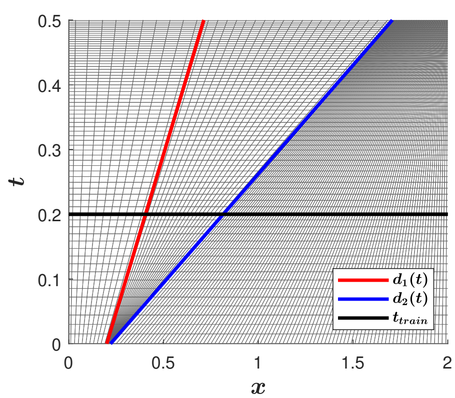

Figure 16: Case 6: Time evolution of the physical mesh for a rarefaction wave generation.

Figure 17 shows solutions computed using the FOM/ROM (left) and CT-FOM/CT-ROM (right). Although the ROM is trained until the final time T, the CT-ROM gives a better approximation to the solution of Case 6. In this rarefaction case, the same conclusions can be drawn as in Case 5 above and the prediction in time is only possible with the CT-ROM.

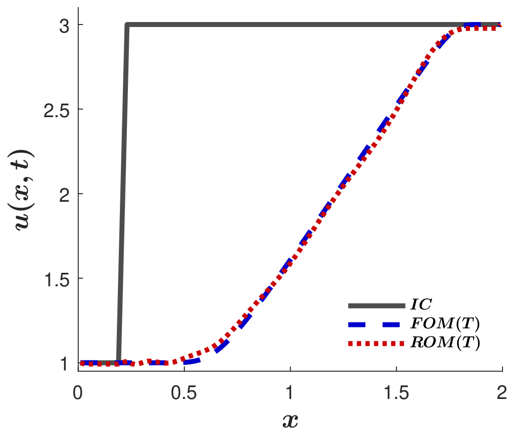

(a) FOM/ROM.

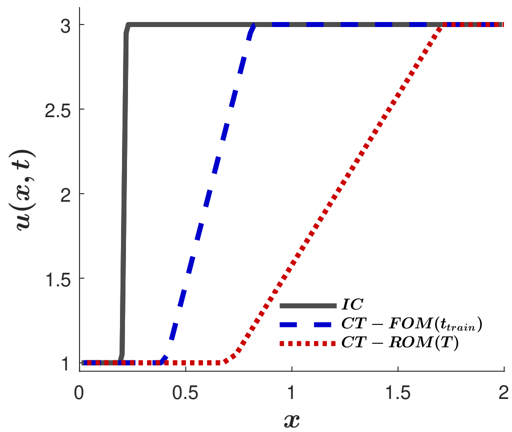

(b) CT-FOM/CT-ROM.

Figure 17: Case 6: Solutions computed with the FOM/ROM (left) and with the CT-FOM/CT-ROM (right).

Finally, Case 7 is considered where the IC of the non-linear problem is not a piecewise linear function. The problem is defined in the domain $[0, 2] \times [0, 0.4]$ and the IC is

$$u(x,0) = \begin{cases} 0, & \text{if } 0 < x \leq d_1(0), \\ \dfrac{(x - d_1(0))x^2}{(d_2(0) - d_1(0))d_2^2(0)}, & \text{if } d_1(0) < x < d_2(0), \\ 1, & \text{if } d_2(0) \leq x \leq 2, \end{cases}$$

where the starting points of the characteristic curves are $d_1(0) = 0.25$ and $d_2(0) = 0.5$ and the BC is

$$u(0,t) = 0, \quad 0 \leq t \leq 0.4.$$

The solution of Case 7 has a raferaction wave and it is approximated with the CT-FOM and the CT-ROM. The spatial domain is divided into $N_x = 128$ volume cells, $CFL = 0.9$, the training time is $t_{train} = 0.1$ and the number of modes is $N_{POD} = 10$. The IC and the computed solutions with both models at the final time $T = 0.4$ are shown in Figure 18. The difference of these solution in ℓ^2 norm is $D_{CT}^{N_T} = 1.799 \cdot 10^{-7}$ and it can be concluded that both solutions for this case are very similar even though the number of modes of the CT-ROM is very small.

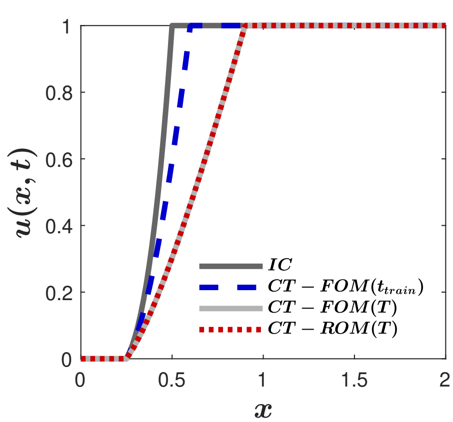

Figure 18: Case 7: Solutions computed with the CT-FOM/CT-ROM.

3.3. 2D extension of the CT-ROM strategy using Radon transform

The CT-ROM strategy introduced in this work is a genuine 1D method. In this section, the CT-ROM strategy is extended to a two-dimensional problem using the Radon transform. The Radon transform is based on the parametrization of any straight line L with respect to the arc length z as

$$\begin{aligned} x(z) &= s\cos\alpha - z\sin\alpha \\ y(z) &= s\sin\alpha + z\cos\alpha, \end{aligned}$$

where s is the distance from L to the origin and α is the angle between L and the y-axis [12, Section 2.2]

The Radon transform of a function f is given by the integral of f along the line L

$$\mathcal{R}f(\alpha, s) = \int_{-\infty}^{+\infty} f(x(z), y(z))dz.$$

The intertwining property of the Radon transform will be of particular interest for the objective of this section. The Radon transform allows to intertwine a partial derivative with a univariate derivative as follows [12, Section 3.6]

$$\mathcal{R}\left\{\frac{\partial f}{\partial x}\right\} = \cos\alpha\,\frac{\partial \mathcal{R}f}{\partial s}, \quad \mathcal{R}\left\{\frac{\partial f}{\partial x}\right\} = \sin\alpha\,\frac{\partial \mathcal{R}f}{\partial s}. \tag{29}$$

Lets consider now the 2D linear homogeneous version of (1), which reads

$$\frac{\partial u}{\partial t} + \lambda_1\frac{\partial u}{\partial x} + \lambda_2\frac{\partial u}{\partial y} = 0, \qquad (x, y, t) \in (-L, L) \times (-L, L) \times (0, T]\,. \tag{30}$$

By applying the intertwining property (29) of the Radon transform to (30), the following set of one-dimensional problems is obtained

$$\frac{\partial \mathcal{R}u}{\partial t} + \hat{\lambda}\frac{\partial \mathcal{R}u}{\partial s} = 0, \qquad (s, t) \in (-L, L) \times (0, T]\,, \tag{31}$$

where $\hat{\lambda} = \lambda_1\cos\alpha + \lambda_2\sin\alpha$, for $\alpha \in (0, \pi)$ [40].

The 1D CT-ROM strategy is used to predict the evolution in time of the 2D hyperbolic problem (30). To do this, first, the IC is transformed from the physical space into the Radon domain, i.e., the (s, α) domain. Then, the CT-ROM strategy described in previous sections is applied to (31) for a discrete collection of values of $\alpha \in (0, \pi)$. Finally, the solution in the (s, α) domain is transformed into the physical space using a filtered back-projection inversion formula for the Radon transform [39, 40]. This is illustrated in the test case described below.

Case 8. 2D transport of Gaussian IC.

Lets consider the problem (30) with $\lambda_1 = \lambda_2 = 1$, $L = 10$ and the final time is $T = 2$. The intervals $[-L, L]$ and $[0, \alpha]$ are uniformly divided into 200 subintervals. The IC is

$$u(x, y, 0) = e^{-\frac{x^2+y^2}{2}},$$

and the BC is

$$u(0, y, t) = u(L, y, t), \quad u(x, 0, t) = u(x, L, t).$$

The CFL number considered in this case is 0.9 and the time step is computed to satisfy the stability condition (16). Solutions are computed with the CT-FOM (14) up to $t_{train} = 0.5$ and, with these data, new solutions are computed using the CT-ROM (15) up to $T = 2$. In this case, a uniform mesh in time is used with step size $\Delta t = 0.05$ to approximate the set of problems (31). Thus, $N_{train} = 10$ and $N_{POD} = 6$.

The numerical solution provided by the CT-ROM at $T = 2$ and the absolute value of the difference between the CT-FOM and the CT-ROM solutions are shown in Figure 19. Note that the position of the center of the CT-FOM solution is marked by a red dot and the IC is also shown. Figure 20 shows the sinogram of the numerical solution provided by the CT-ROM, i.e., the solution in the (s, α) plane. The contourline corresponding to the maximum value of the sinogram of the CT-FOM solution is also depicted using a red line, showing a good agreement between both solutions. These results evidence that although the CT-ROM strategy herein proposed is a genuine method for 1D time dependent problems, it can be extended to higher spatial dimensions using the Radon transform.

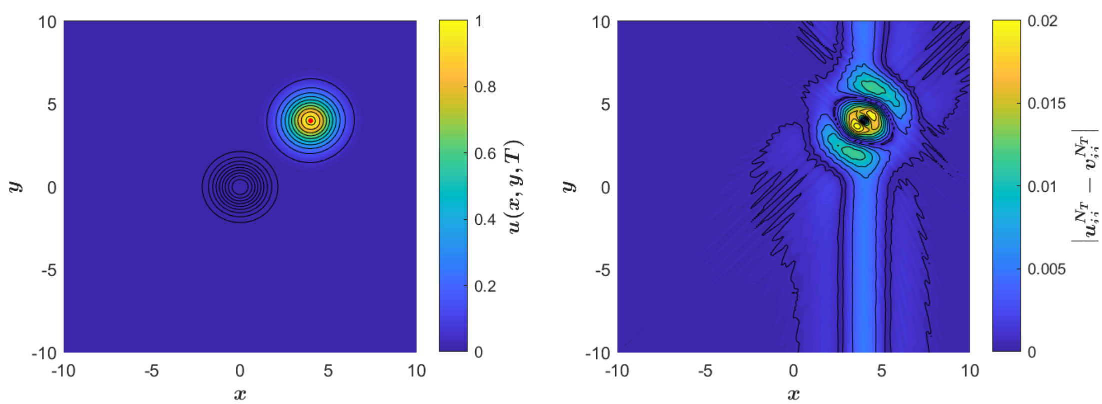

(a) Solution of the CT-ROM.

(b) CT-FOM vs. CT-ROM.

Figure 19: Case 8: Solution computed with the CT-ROM and its comparison with the CT-FOM.

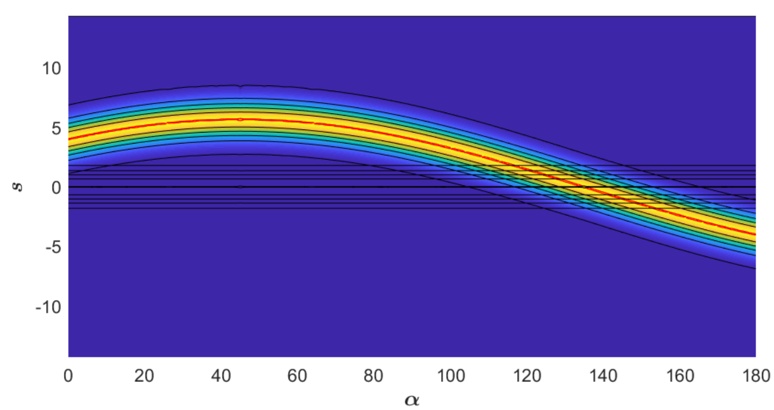

Figure 20: Case 8: Sinogram of the numerical solution at $T = 2$.

In the case of a 2D non-linear equation, it would be necessary to perform the Radon transformation and then take into account the considerations set out in section 3.2 and

Cases 5, 6 and 7.

4. Concluding remarks

The standard POD-based ROM strategy for the resolution of partial differential equations allows extrapolation in time when the equation of interest is not advection-dominated. In the case of hyperbolic problems, or other more general advection-dominated problems, the standard POD-based ROM fails when computing the solution beyond the training time.

In this work, a new ROM strategy that allows the prediction of solutions beyond the training time, called CT-ROM, is proposed. The CT-ROM strategy is based on a coordinate transformation using characteristic curves [19]. This novel approach has been assessed using a variety of eight different test cases that comprise a variety of scenarios. The proposed cases have been designed to analyze the CT-ROM response to different characteristics and configurations, showing promising results in all of the scenarios considered. These problems include 1D linear advective equations with diffusion and reaction source terms, systems of coupled linear equations, including the linearized shallow water equations, and the non-linear inviscid Burgers' equation. The numerical results evidence the prediction capability of the CT-ROM strategy. This achievement is presented here for the first time, to the knowledge of the authors.

On the one hand, linear problems allow a direct application of the CT-ROM strategy, obtaining accurate solutions for larger times than the training times (Cases 1, 2 and 3). Linear systems such as the linearized shallow water equations have to be decoupled so that each new variable evolves in its own domain following the proposed coordinate transformation (Case 4). On the other hand, it has been observed that the non-linearity of the equations challenges the prediction capabilities of the CT-ROM strategy. This is the case of Burgers' equation (Cases 5, 6 and 7). The generation of shock and rarefaction waves requires the division of the domain into sub-domains. In this way, this limitation can be addressed and high accuracy solutions can be obtained. For more complex ICs than those of the cases described here, the suggested procedure would be to further subdivide the domain.

The CT-ROM strategy is based on a coordinate transformation only valid for 1D problems. An extension of the CT-ROM to 2D based on the Radon transform has been proposed (Case 8). By means of the intertwining property of the Radon transform, the problem can be reduced to a set of 1D problems, thus making possible the application of the the CT-ROM to each of them. The results of Case 8 show the effective combination of both transformations, allowing the extrapolation of solutions beyond the training time with high accuracy.

Acknowledgements

The authors would like to express their gratitude to Dr. Donsub Rim for interesting discussions on reduced-order models. This work was funded by the Spanish Ministry of Science and Innovation under the research project PGC2018-094341-B-I00. This work has also been partially funded by Gobierno de Aragón through Fondo Social Europeo (T32-20R and E24-17R, Feder 2019-2021 "Construyendo Europa desde Aragón").

References

[1] M. Ahmed and O. San. Stabilized principal interval decomposition method for model reduction of nonlinear convective systems with moving shocks. Comput. Appl. Math., 37:6870–6902, 2018.

[2] S.E. Ahmed, O. San, D.A. Bistrian, and I.M. Navon. Sampling and resolution characteristics in reduced order models of shallow water equations: Intrusive vs nonintrusive. Int. J. Numer. Methods Fluids, 92(8):992–1036, 2020.

[3] I. Akhtar, Z. Wang, J. Borggaard, and T. Iliescu. A new closure strategy for proper orthogonal decomposition reduced-order models. J. Comput. Nonlinear Dyn., 7(3), 04 2012. 034503.

[4] F. Alcrudo and P. Garcia-Navarro. A high-resolution Godunov-type scheme in finite volumes for the 2D shallow-water equations. Int. J. for Numer. Methods Fluids, 16(6):489–505, 1993.

[5] B.O. Almroth, P. Stern, and F.A. Brogan. Automatic choice of global shape functions in structural analysis. AIAA Journal, 16(5):525–528, 1978.

[6] M. Barrault, Y. Maday, N.C. Nguyen, and A.T. Patera. An 'empirical interpolation' method: application to efficient reduced-basis discretization of partial differential equations. C. R. Math., 339(9):667–672, 2004.

[7] J. Borggaard, A. Hay, and D. Pelletier. Interval-based reduced-order models for unsteady fluid flow. Int. J. Numer. Anal. Model., 4:353–367, 2007.

[8] J. Burguete, P. García-Navarro, and J. Murillo. Preserving bounded and conservative solutions of transport in one-dimensional shallow-water flow with upwind numerical schemes: Application to fertigation and solute transport in rivers. Int. J. Numer. Methods Fluids, 56(9):1731–1764, 2008.

[9] S. Chaturantabut and D.C. Sorensen. Discrete empirical interpolation for nonlinear model reduction. In Proceedings of the 48h IEEE Conference on Decision and Control (CDC) held jointly with 2009 28th Chinese Control Conference, pages 4316–4321, 2009.

[10] E.A. Christensen, M. Brøns, and J.N. Sørensen. Evaluation of proper orthogonal decomposition–based decomposition techniques applied to parameter-dependent nonturbulent flows. SIAM J. Sci. Comput., 21(4):1419–1434, 1999.

[11] R. Courant, K. Friedrichs, and H. Lewy. Über die partiellen Differenzengleichungen der mathematischen Physik. Math. Ann., 100(1):32–74, 1928.

[12] S.R. Deans. The Radon transform and some of its applications. A Wiley-Interscience Publication. John Wiley & Sons, Inc., New York, 1983.

[13] P. Feldmann and R.W. Freund. Efficient linear circuit analysis by Pade approximation via the Lanczos process. In Proceedings of the Conference on European Design Automation, EURO-DAC '94, page 170–175, Washington, DC, USA, 1994. IEEE Computer Society Press.

[14] B.G. Galerkin. Rods and plates. Series occurring in various questions concerning the elastic equilibrium of rods and plates. Engineers Bulletin (Vestnik Inzhenerov), 19:897 – 908, 1915.

[15] R. Garcia and R.A. Kahawita. Numerical solution of the St. Venant equations with the MacCormack finite-difference scheme. Int. J. Numer. Methods Fluids, 6(5):259–274, 1986.

[16] P. Garcia-Navarro and M.E. Vazquez-Cendon. On numerical treatment of the source terms in the shallow water equations. Comput. Fluids, 29(8):951–979, 2000.

[17] S.K. Godunov and I. Bohachevsky. Finite difference method for numerical computation of discontinuous solutions of the equations of fluid dynamics. Matematičeskij Sbornik, 47(89)(3):271–306, 1959.

[18] G.H. Golub and C.F. Van Loan. Matrix Computations. Johns Hopkins Studies in the Mathematical Sciences. Johns Hopkins University Press, 2013.

[19] J.L. Gracia and E. O'Riordan. A singularly perturbed convection-diffusion problem with a moving interior layer. Int. J. Numer. Anal. Model., 9(4):823–843, 2012.

[20] M.A. Grepl and A.T. Patera. A posteriori error bounds for reduced-basis approximations of parametrized parabolic partial differential equations. ESAIM Math. Model. Numer. Anal., 39:157–181, 2005.

[21] P. Holmes, J.L. Lumley, and G. Berkooz. Turbulence, Coherent Structures, Dynamical Systems and Symmetry. Cambridge Monographs on Mechanics. Cambridge University Press, 1996.

[22] W.L. IJzerman. Signal Representation and Modeling of Spatial Structures in Fluids. PhD thesis, University of Twente, April 2000.

[23] I.T. Jolliffe. Principal Component Analysis. Springer Series in Statistics. Springer, 2002.

[24] K. Karhunen. Über lineare Methoden in der Wahrscheinlichkeitsrechnung. Ann. Acad. Sci. Fennicae. Ser. A. I. Math.-Phys., 37:1–79, 1947.

[25] R.J. LeVeque. A well-balanced path-integral f-wave method for hyperbolic problems with source terms. J. Sci. Comput., 58:209–226, 2011.

[26] M. Loève. Probability theory. The University Series in Higher Mathematics. D. Van Nostrand Co., Inc., Princeton, N. J.-Toronto-New York-London, 1960. 2nd ed.

[27] J.L. Lumley. The structure of inhomogeneous turbulent flows. Atmospheric Turbulence and Radio Wave Propagation, pages 166–176, 1967.

[28] J. Murillo and P. García-Navarro. Weak solutions for partial differential equations with source terms: Application to the shallow water equations. J. Comput. Phys., 229(11):4327 – 4368, 2010.

[29] D.A. Nagy. Modal representation of geometrically nonlinear behavior by the finite element method. Comput. Struct., 10(4):683–688, 1979.

[30] A. Navas-Montilla, P. Solán-Fustero, J. Murillo, and P. García-Navarro. Discontinuous Galerkin well-balanced schemes using augmented Riemann solvers with application to the shallow water equations. J. Hydroinformatics, 04 2020. jh2020206.

[31] N.C. Nguyen, G. Rozza, and A.T. Patera. Reduced basis approximation and a posteriori error estimation for the time-dependent viscous Burgers' equation. Calcolo, 46:157–185, 2009.

[32] A.K. Noor and J.M. Peters. Reduced basis technique for nonlinear analysis of structures. AIAA Journal, 18(4):455–462, 1980.

[33] C. Parés and M. Castro. On the well-balance property of Roe's method for nonconservative hyperbolic systems. Applications to shallow-water systems. ESAIM Math. Model. Numer. Anal., 38(5):821–852, 2004.

[34] K. Pearson. LIII. On lines and planes of closest fit to systems of points in space. The London, Edinburgh, and Dublin Philosophical Magazine and Journal of Science, 2(11):559–572, 1901.

[35] C. Prud'Homme, D.V. Rovas, K. Veroy, L. Machiels, Y. Maday, A.T. Patera, and G. Turinici. Reliable real-time solution of parametrized partial differential equations: Reduced-basis output bound methods. J. Fluids Eng., 124(1):70–80, November 2001.

[36] A. Quarteroni, A. Manzoni, and F. Negri. Reduced basis methods for partial differential equations: An introduction, volume 92 of Unitext. Springer, Cham, 2016.

[37] A. Quarteroni, G. Rozza, L. Dedè, and A. Quaini. Numerical approximation of a control problem for advection-diffusion processes. In F. Ceragioli, A. Dontchev, H. Futura, K. Marti, and L. Pandolfi, editors, System Modeling and Optimization, pages 261–273, Boston, MA, 2006. Springer US.

[38] J. Radon. On the determination of functions from their integral values along certain manifolds. IEEE Trans. Med. Imaging, 5(4):170–176, 1986.

[39] D. Rim. Dimensional splitting of hyperbolic partial differential equations using the Radon transform. SIAM J. Sci. Comput., 40(6):A4184–A4207, 2018.

[40] D. Rim, B. Peherstorfer, and K.T. Mandli. Manifold approximations via transported subspaces: Model reduction for transport-dominated problems. ArXiv, 1912.13024, 2020.

[41] D. V. Rovas, L. Machiels, and Y. Maday. Reduced-basis output bound methods for parabolic problems. IMA J. Numer. Anal., 26(3):423–445, 2006.

[42] O. San and T. Iliescu. Proper orthogonal decomposition closure models for fluid flows: Burgers equation. ArXiv, 1308.3276, 2013.

[43] P.J. Schmid. Dynamic mode decomposition of numerical and experimental data. J. Fluid Mech., 656:5–28, 2010.

[44] L. Sirovich. Turbulence and the dynamics of coherent structures. I - Coherent structures. II - Symmetries and transformations. III - Dynamics and scaling. Q. Appl. Math., 45:561–571,573–582, 583–590, 1987.

[45] T. Taddei, S. Perotto, and A. Quarteroni. Reduced basis techniques for nonlinear conservation laws. ESAIM Math. Model. Numer. Anal., 49(3):787–814, 2015.

[46] A. Towne, O. T. Schmidt, and T. Colonius. Spectral proper orthogonal decomposition and its relationship to dynamic mode decomposition and resolvent analysis. J. Fluid Mech., 847:821–867, 2018.

[47] Julien Weiss. A tutorial on the proper orthogonal decomposition. AIAA Aviation Forum. June 2019.

[48] J.-M. Zokagoa and Soulaïmani A. A POD-based reduced-order model for uncertainty analyses in shallow water flows. Int. J. Comput. Fluid Dyn., 32(6-7):278–292, 2018.